Canted stripe phase near the spin reorientation transition in ultrathin magnetic films

J. P. Whitehead,[1] A. B. MacIsaac,[2,*] and K. De'Bell[3]

[1]*Department of Physics and Physical Oceanography, Memorial University of Newfoundland, St John's, Newfoundland, Canada A1B 3X7*

[2]*Department of Applied Mathematics, University of Western Ontario, London, Canada N6A 5B7*

[3]*Mathematical Sciences Department, University of New Brunswick at Saint John, Saint John, Canada E2L 4L5*

(Received 26 November 2007; revised manuscript received 15 April 2008; published 9 May 2008)

Results from computer simulation and numerical studies for the ferromagnetic Heisenberg model on a square lattice are presented. The model includes the exchange and dipolar interactions as well as the magnetic anisotropy. The analysis focuses on the nature of the stripe phase which determines the phase behavior of this system close to the reorientation transition for a particular value of the exchange constant corresponding to $\mathcal{J}=8.9$ in reduced units. The results show that as the perpendicular anisotropy parameter κ is increased from zero, the system undergoes a reorientation transition from the planar ferromagnetic phase to the stripe phase. Both the simulations and ground state calculations show that the stripe phase consists of two distinct regions. For large values of κ, the spins are aligned, on average, perpendicular to the plane with properties qualitatively similar to those observed for the dipolar Ising model. Close to the reorientation transition, there exists a narrow range of κ in which the perpendicular components of the spins align to form stripes, but with the spins canted toward the plane giving rise to a net transverse magnetization. We present a phase diagram based on the results from the numerical calculations and simulation studies and discuss connections with earlier theoretical and simulation studies, as well as experiments on ultrathin magnetic films. In particular, we draw attention to similarities between the results presented in this study and the so-called temperature gap (or pseudogap) region observed experimentally at the reorientation transition in ultrathin magnetic films. We also discuss the extent to which the results of these studies support the conclusion that the three types of magnetic order observed in these studies represent distinct thermodynamic phases.

DOI: 10.1103/PhysRevB.77.174415 PACS number(s): 75.70.Ak, 75.10.Hk, 75.30.Kz, 75.40.Mg

I. INTRODUCTION

Ultrathin magnetic films (UTMFs) consist of several, typically $\lesssim 10$, layers of magnetic atoms deposited on a nonmagnetic substrate. Advances in the fabrication and characterization of epitaxially grown thin films have allowed researchers to fabricate films consisting of multiple layers, each with a distinct and well defined atomic structure. By carefully selecting the substrate, the atomic composition, and number of layers, it is possible to produce materials that exhibit a fascinating and diverse range of magnetic properties. Such materials are of obvious fundamental scientific interest and are of considerable technological significance.[1]

The ability to finely tune the magnetic properties of these materials by varying the number and composition of the layers makes it possible to create magnetic materials in which the magnetic moments are aligned perpendicular or parallel to the surface.[2–12] This can give rise to an experimentally observed reorientation transition, where the orientation of the magnetic moments changes depending on the number of layers or the temperature[2,5,7,11,12] and which has been studied both analytically[13] and by numerical simulation.[14,15]

A number of systems with a net magnetization perpendicular to the plane have been shown experimentally to manifest a stripe domain phase consisting of elongated microdomains of alternating magnetization direction.[3,5,7–11,16] The characteristic width of these microdomains can vary significantly as a function of film thickness, applied field, and temperature and can extend over a wide range of length scales. The formation of these stripe phases is reasonably well understood theoretically as arising from the competition between the short range exchange interaction and the long-range anisotropic dipolar interaction,[17–20] and there are instances of good quantitative agreement between experiment and certain theoretical models.[16]

Magnetic imaging experiments also show that in some cases, the stripes are orientated along a common direction,[9,11,16] while in other cases, the stripes are observed to exhibit a more complex structure with no orientational ordering.[3,7,9] The transition from an orientationally ordered stripe phase to one in which the stripes are orientationally disordered has been observed in experiments[9] and simulations[21] and studied theoretically.[22,23] However, while there exist qualitative similarities between the results of simulation, theory, and experiment, the precise nature of this transition is still poorly understood.

There are other aspects of these materials for which a complete understanding remains elusive. For example, close to the reorientation transition, experiments show that a gap exists between the temperature at which the perpendicular component of the magnetization disappears and the transverse component is observed.[6,7,12] It has been conjectured that this gap region is not associated with the loss of long-range magnetic order but instead manifests a complex magnetic structure that cannot be resolved experimentally.[12] This conjecture is supported by imaging experiments,[7] which show a rapid decrease in the stripe width in the neighborhood of the reorientation transition. Unfortunately, previous theoretical and simulation studies offer few insights regarding the precise nature of the phase behavior in this temperature region.

There are also a number of experimental studies on the magnetic susceptibility of UTMFs which indicate a very

strong relationship between the magnetic response of these materials and the properties of the stripe phase; however, we do not have a complete theoretical description.[5,10,24–26]

From a theoretical perspective, this gap in our understanding arises because it is difficult to connect the results obtained from the various approaches which have been used to explain different aspects of the observed properties of these systems. For example, while the formation of the stripes in the perpendicular magnetization and their behavior at finite temperature and in an applied field can be described in terms of the dipolar Ising model, such a model ignores the effect of the transverse magnetization and the structure of the walls separating the stripes. Both of these aspects are important if we are to account for the reorientation transition observed in these systems, the effects of film thickness and magnetic surface anisotropy on the properties of the spatial morphology of the magnetic structure, and the pinning mechanisms that determine the magnetic response of these materials. On the other hand, while the more general dipolar Heisenberg model provides a more complete description of the effects of surface anisotropy and the structure of the stripe walls and reduces to the Ising model in the appropriate limits, it is a much more difficult model to extend to finite temperature. While there have been a number of simulation studies published based on the dipolar Heisenberg model, they extend over a rather limited range of parameters[27] or used an inappropriate sampling method.[28–30]

In the present work, we present a series of simulation studies of the dipolar Heisenberg model together with some analytical calculations. The results of the study connect with a number of other numerical and theoretical studies, provide a number of results, correct previous work, and provide the beginnings of an approach that has the potential to provide a more complete and consistent approach to these materials and that, unlike the dipolar Ising model, can reproduce the results of important limiting cases.

Model

We consider a system of classical spins each with a magnetic moment μ_{eff}. The spins are located on the vertices of a square lattice with lattice constant a and interact through a nearest neighbor exchange and a dipolar interaction as well as a single site anisotropy. The Hamiltonian of a given spin configuration $\{\vec{\sigma}_i\}$ may be written in terms of dimensionless parameters as

$$\mathcal{H} = -\mathcal{J}\sum_{\langle ij\rangle} \vec{\sigma}_i \cdot \vec{\sigma}_j + \sum_{i\neq j}\left(\frac{\vec{\sigma}_i\cdot\vec{\sigma}_j}{|\vec{r}_{ij}|^3} - 3\frac{(\vec{\sigma}_i\cdot\vec{r}_i)(\vec{\sigma}_j\cdot\vec{r}_j)}{|\vec{r}_{ij}|^5}\right) - \kappa\sum_i (\sigma_i^z)^2, \tag{1}$$

where $\vec{\sigma}_i$ denotes a unit vector that describes the orientation of the ith spin and $\vec{r}_i$ denotes the location of the ith spin on a square lattice with lattice parameter equal to 1 and where $\langle ij\rangle$ represents a sum over all pairs of nearest neighbor spins and $i\neq j$ represents a sum over all pairs of spins. The constants $\mathcal{J}$ and κ represent the strength of the exchange constant and the on-site magnetic anisotropy, respectively, in dimensionless units. We assume that the z axis is perpendicular to the surface and that the x and y axes are aligned along the lattice axes.

At $\kappa=\infty$, the system reduces to the dipolar Ising model, although exactly how the system approaches this limit is an open question. In the case of the dipolar Ising model, it is well known that the dipolar interaction destabilizes the ferromagnetic ground state giving rise to a perpendicular stripe phase with several rows of spins aligned ferromagnetically, but with a direction that alternates with some period $2h$. The period $2h\propto e^{\mathcal{J}/4}$ in the limit $\mathcal{J}\to\infty$, with a ground state energy (per spin) given by[31]

$$E = -2\mathcal{J} + \left(9.034 - \frac{8}{h}\right) - \kappa. \tag{2}$$

While the expressions for h and E are, strictly speaking, correct in the limit $h\to\infty$, it should be noted that these expressions are surprisingly accurate even for moderate values of $h\gtrsim 4$.[20,32–34]

For small values of κ and $\mathcal{J}>0.28$,[35] the ground state is ferromagnetic with the spins aligned in the plane and oriented along either the x or the y axis. The energy of the planar ground state is given by

$$E = -2\mathcal{J} - 4.517. \tag{3}$$

A comparison of the ground state energies for the perpendicular stripe phase and the planar ferromagnetic phase indicates a transition at $\kappa=12.55$ from the perpendicular stripe phase to the transverse ferromagnetic phase.[20,34,36]

In Sec. II, we begin by presenting results from simulations at $T=0.05$, for $\kappa=20$ and 0. We compare results of the simulations for $\kappa=20$ with previously published results for the Ising model. Simulations for $\kappa=13.0$ at $T=0.5$, just above the reorientation transition, are presented for different initial spin configurations. While there are issues regarding the equilibration times related to the different initial conditions, the simulations nevertheless provide compelling evidence that the system evolves toward an equilibrium in which the perpendicular components of the spins align to form stripes, but with the spins canted toward the plane giving rise to a net transverse magnetization.

In Sec. III, we describe how the ground state spin configuration may be calculated based on certain assumptions regarding the periodic nature of the ground state. Ground state spin configurations are presented for $\mathcal{J}=8.9$ for several values of κ and the resultant ground state energy and transverse magnetization plotted as a function of κ. These results show that for $\mathcal{J}=8.9$, the model yields three distinct ground state spin configurations which we refer to as the planar ferromagnetic, canted stripe, and perpendicular stripe spin configurations. The results obtained from the ground state calculation are consistent with the results from the simulations presented in Sec. II. Results are presented that show the equilibrium stripe width of the canted stripe phase depends on κ, becoming smaller as κ is decreased, qualitatively consistent with previous theoretical work.[18]

In Sec. IV, we present the results of a series of simulation studies for a range of temperatures and κ. The results of these simulations are combined with the results of the previous section to construct a preliminary phase diagram for the model. We finish by discussing the conclusions that may be drawn from the results presented in the preceding sections.

II. SIMULATION STUDIES

In this section, we present the results of a series of simulation studies for $\mathcal{J}=8.9$ at three representative values of κ: $\kappa=20$, 13, and 0. The intention is that these three values of κ will be sufficient to identify the various regions in the phase diagram. We first summarize the properties of the three regions briefly before we provide a more detailed analysis.

For $\kappa=20$, the anisotropy is sufficiently large that the system exhibits many of the features of the dipolar Ising model. It has a ground state in which the spins are aligned perpendicular to the plane but which exhibits a periodic structure consisting of stripes of width $h=8$ oriented along either the x or the y axis with the magnetization in adjacent stripes aligned antiparallel. As the temperature is increased, the orientational order of the stripes decreases until, as in the case of the dipolar Ising model, the system undergoes a transition to the tetragonal phase.[21]

For $\kappa=0$, the ground state is ferromagnetic with the spins aligned in the plane of the film and oriented along either the x or the y axis. As the temperature is increased, the magnetization decreases until we reach the Curie temperature T_c, at which point the magnetization is zero and the system makes the transition to the paramagnetic phase.

For $\kappa=13.0$, at low temperature ($T=0.5$), the results from the simulations show that the system also orders to form stripes in the perpendicular component of the magnetization; however, the nature of the order is such that the magnetization is not completely aligned perpendicular to the plane but is canted toward it in the direction of the stripes. In addition, unlike the results for the dipolar Ising system, the walls separating the stripes acquire a finite width in which the spins align to form a transverse ferromagnetic region. Hence, while the nonequilibrium relaxation is very slow, the results nevertheless indicate that, in equilibrium, the magnetic order manifests both orientationally ordered stripes perpendicular to the plane together and a net transverse magnetization.

The Monte Carlo results presented in this paper are derived from simulations of a system of $N=128\times128$ spins on a square lattice, where the long-range nature of the dipole-dipole interaction is treated by assuming one has an infinite system composed of replicas of the base 128×128 system. Ewald summation techniques are then used to map the full dipole-dipole interaction to the finite system. For the exchange interaction, this is equivalent to periodic boundary conditions. Further details on this aspect of treating the dipolar interaction are available in the work MacIsaac *et al.*[32] The actual simulation code is written using message passing interface directives such that the code can be efficiently run on parallel machines. The efficiency depends on system size (the larger the system, the higher the efficiency), and sufficiently high efficiency rates have been achieved by using domain decomposition of the effective fields, while each process maintains a full, up to date spin state and each process generates its own equivalent stream of random numbers. On small SMP machines (up to four way), superscalar speedups are possible, even with a system size of $N=128\times128$.[37] A typical simulation involves on the order of 10^5-10^6 Monte Carlo steps (MCSs) to allow the system to reach equilibrium followed by an additional 10^5-10^7 MCSs with data taken from every 10th or 20th MCS, depending upon the temperature of the simulation. A Monte Carlo step is defined as N attempted spin updates. In all the work presented, the Metropolis algorithm was used to update the spins. It is important to note that the nonequilibrium relaxation times in these systems can be very long and great care must be taken to ensure that the system has reached equilibrium before taking data.[38,39]

A. Perpendicular stripes ($\kappa=20.0$)

We first consider in more detail the case of large single site anisotropy, $\kappa=20$, which is expected to have properties similar to that found by Booth *et al.* for the two-dimensional dipolar Ising model. Extensive simulations were carried out, each starting with an initial spin configuration consisting of perpendicular stripes of width $h=8$. Snapshots of spins configurations at several temperatures are show in Fig. 1. The configurations are indeed qualitatively similar to those obtained for the dipolar Ising model.[21] In particular, at low temperature, $T=2.0$ and 3.0, the spins form ferromagnetic stripes of width $h\approx8$ which are oriented along the x axis. As the temperature is increased to $T=3.5$, the stripes are still clearly aligned along a common axis but exhibit a number of isolated defects. Around $T=4.0$, the stripes disorder, losing their orientational order analogous to the smectic $\rightarrow$tetragonal phase transition observed in the dipolar Ising model. As the temperature is increased further, we see the stripes begin to thin and break up.

In order to make a more systematic comparison with the results of Booth *et al.*, we generalize the definition of the orientational order parameter O_{hv} defined in Ref. 21 as

$$O_{hv}=\frac{n_h-n_v}{n_h+n_v}, \tag{4}$$

where n_h and n_v denote the number of antiferromagnetic bonds in the horizontal and the vertical direction, respectively. In order to accommodate the continuous nature of the Heisenberg spins, we redefine n_h and n_v as

$$n_h=\sum_{\vec{r}}^{L^2}[1-\vec{\sigma}(\vec{r})\cdot\vec{\sigma}(\vec{r}+\hat{x})], \tag{5}$$

$$n_v=\sum_{\vec{r}}^{L^2}[1-\vec{\sigma}(\vec{r})\cdot\vec{\sigma}(\vec{r}+\hat{y})], \tag{6}$$

where the sums are over all lattice points. These generalizations of n_h and n_v reduce to the expressions defined in the work of Booth *et al.* in the case of the dipolar Ising model and provide an appropriate measure of the orientational order in the Heisenberg model.

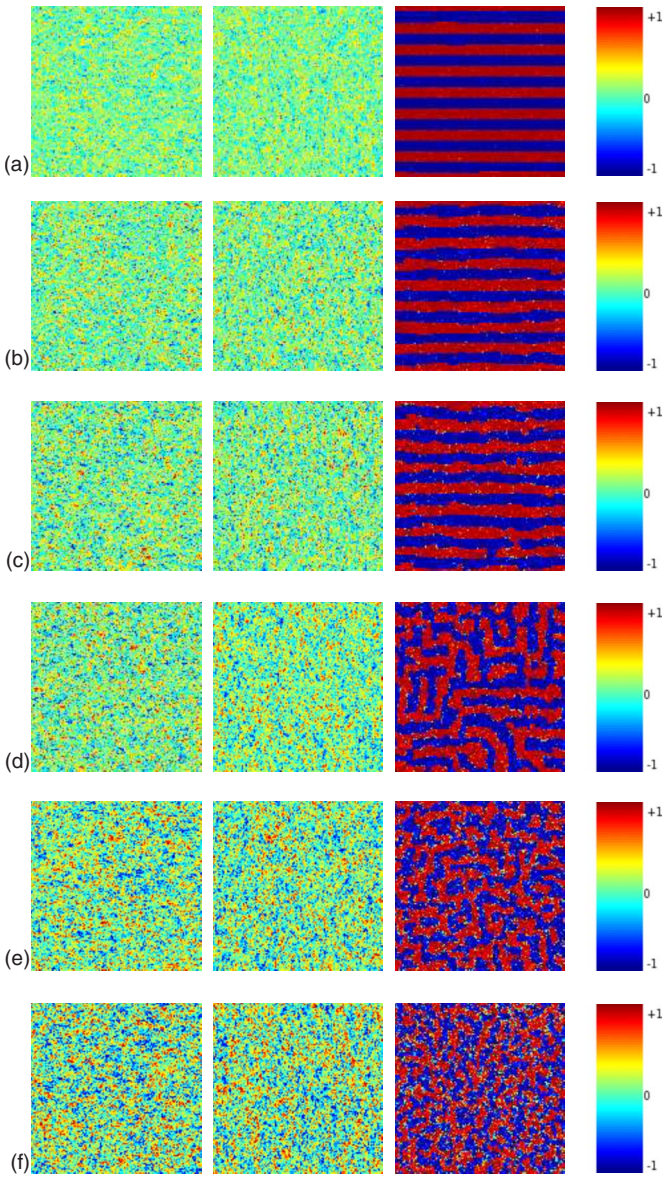

FIG. 1. (Color online) Configurations showing the x, y, and z components of the spins from a simulation with $\kappa=20$. (a) $T=2.0$, (b) $T=3.0$, (c) $T=3.5$, (d) $T=4.0$, (e) $T=5.0$, and (f) $T=6.0$ together with the color map used to show the components of the spins.

In Figs. 2(a) and 2(b), we show the variation of O_{hv} as a function of temperature for the dipolar Heisenberg model and the dipolar Ising model, respectively. We note that the results are qualitatively similar, although in the case of the dipolar Heisenberg model, the thermal excitation of the spin wave modes gives rise to a linear dependence of the orientational order parameter at low temperature. In Fig. 2(a), we observe that the orientation order parameter indicates a phase transition for $\kappa=20$ at $T\approx 3.8\pm 0.1$, which is lower than corresponding transition temperature in the case of the dipolar Ising model which occurs at $T\approx 5.1\pm 0.1$. Evidence for the transition from the smectic to the tetragonal phase is also seen in the peak of the heat capacity presented in Fig. 3. The corresponding data for the dipolar Ising model are also presented.

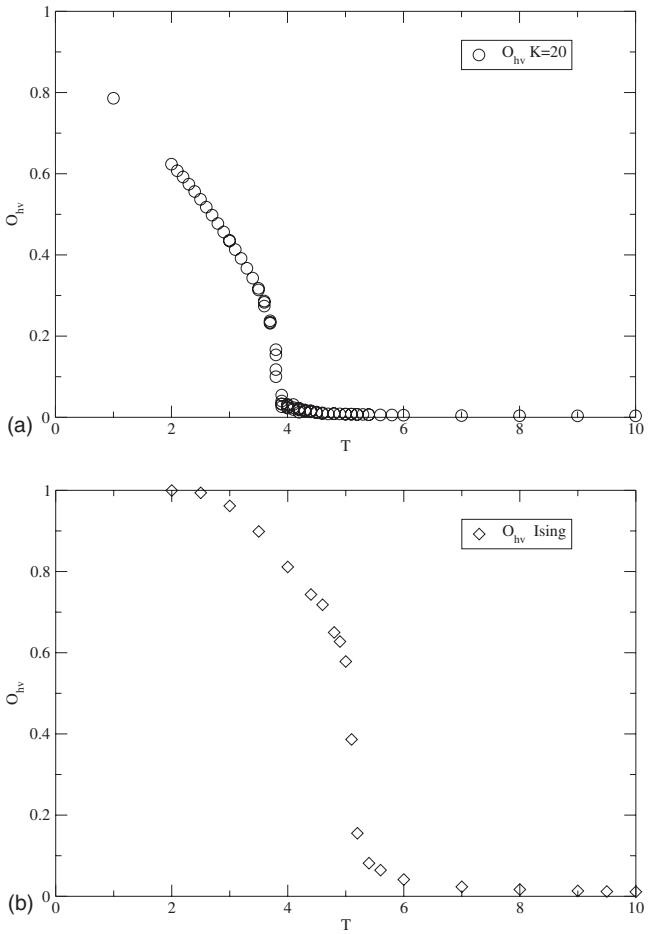

FIG. 2. Plot of the orientational order parameter O_{hv} for (a) the dipolar Heisenberg model with $\kappa=20.0$ and (b) the dipolar Ising model.

B. Transverse ferromagnetism ($\kappa=0.0$)

We now consider the case $\kappa=0$. In our simulations, we have used the transverse ferromagnetic ground state with the spins aligned along the x axis as the initial spin configuration. The magnetization is plotted as a function of temperature in Fig. 4(a). We define the magnetization and the transverse magnetization, M and M_t, respectively, as the ensemble averages,

$$M = (\langle M_x\rangle^2 + \langle M_y\rangle^2 + \langle M_z\rangle^2)^{1/2}, \tag{7}$$

$$M_t = (\langle M_x\rangle^2 + \langle M_y\rangle^2)^{1/2}. \tag{8}$$

M_x, M_y, and M_z are sums over the entire lattice of the respective spin components for a given spin configuration, normalized by the number of spins. The results show a linear decrease in the magnetization with temperature due to the spin wave fluctuations at low temperature ($T\lesssim 6.5\pm 0.5$), with the magnetization dropping effectively to zero at $T_c\approx 9.0\pm 0.2$. The transition to the paramagnetic phase at T_c is also reflected in Fig. 4(b), where we plot the specific heat as a function of temperature. The data show a well defined peak around T_c consistent with a transition from the ferromagnetic to the paramagnetic phase.

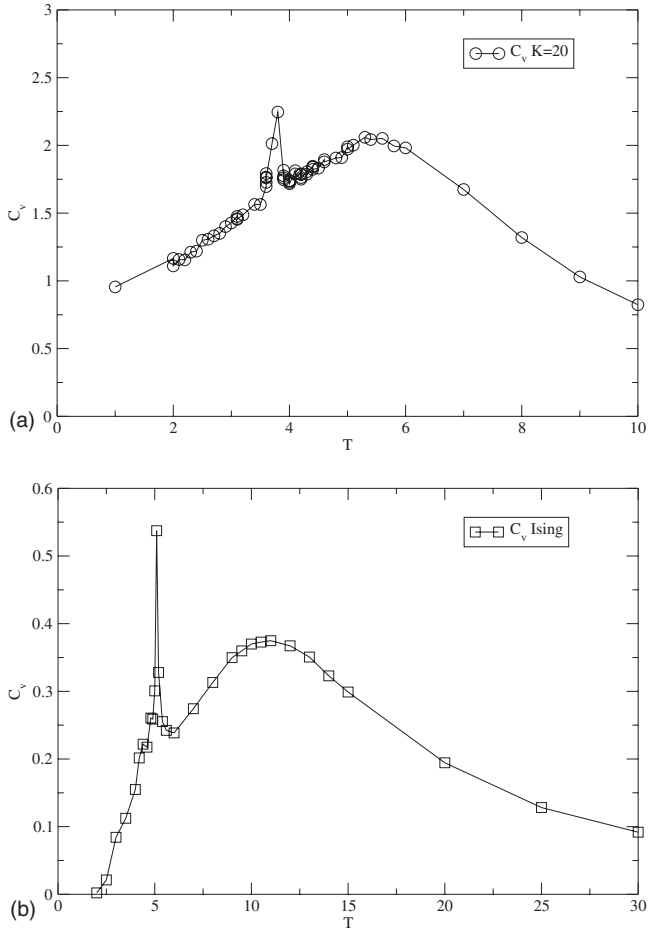

FIG. 3. Plot of the heat capacity C_v for (a) the Heisenberg model with $\kappa=20.0$ and (b) the dipolar Ising model. Lines connect successive points as a guide to the eye.

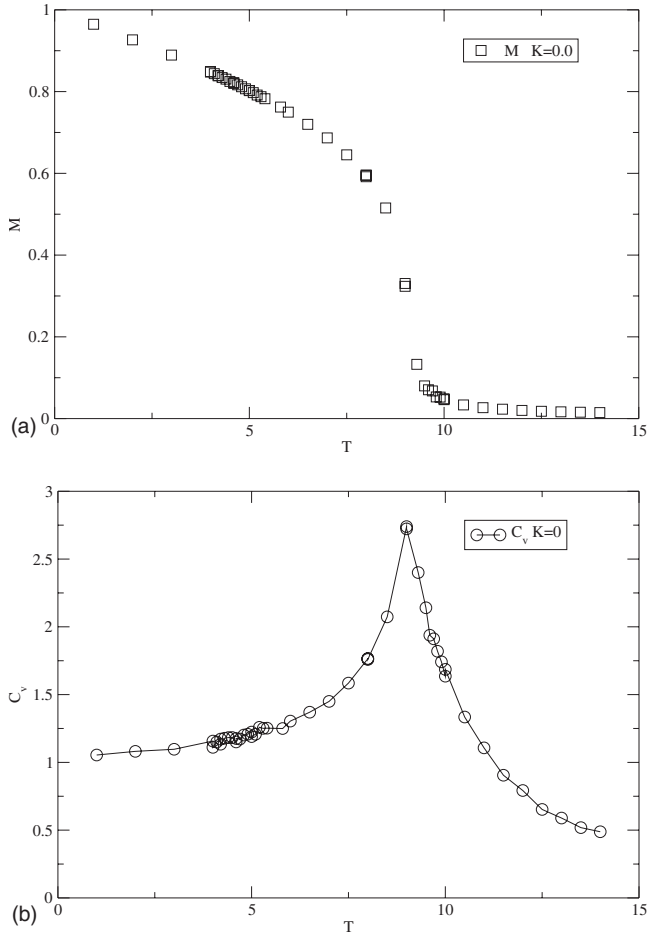

FIG. 4. Plot of (a) the magnetization and (b) the specific heat for the dipolar Heisenberg model with $\kappa=0.0$. Lines connect successive points as a guide to the eye.

C. Canted stripes ($\kappa=13.0$)

For $\kappa=13.0$, we present results from three separate quenches, each with a different initial spin configuration, for $T=0.5$. Our simulations reveal that the nature of the equilibrium magnetic order is somewhat more complicated to determine than one might initially suppose.

In the first set of simulations, we used as our initial spin configuration perpendicular stripes with $h=8$. Snapshots of several spin configurations at increasing times are presented in Fig. 5.

The results from the simulation manifest a number of interesting features. In Fig. 5(c), we note that while the periodic structure of the initial spin configuration persists, the nature of the stripes becomes more complex with the walls separating the stripes acquiring a finite width and the spins inside the domain walls tilting toward the plane. Comparing Figs. 5(c) and 5(d), we see that as the system evolves further, the spins in the stripe walls align along a common direction, until at $t=1\times10^6$ MCSs when the system consists of two distinct domains, one with the spins in the stripe walls tilted along the positive x direction and the other with the spins in the stripe walls tilted along the negative x direction. In order to illustrate the nature of the spin configuration more clearly, Fig. 6 shows a plot of the magnetization vector, averaged along the x axis (parallel to the stripes), plotted as a function of the y coordinate (normal to the stripes), for the spin configuration shown in Fig. 5(d). Figure 6(a) plots the three components of the average, while Fig. 6(b) plots the angle the average makes with respect to the y coordinate.

Figure 6 clearly shows that the system has evolved such that the spins inside each stripe wall are tilted along the x axis and the stripe walls manifest a net transverse magnetization, with one domain in which the magnetization is in the positive x direction and another in the negative x direction. We expect that the system will eventually evolve into a single domain, with one domain growing at the expense of the other; however, the equilibration times for such a process are obviously extremely long. It is also interesting to note the similarity between the domain structure shown in Fig. 5(d) and the experimental results shown in Fig. 1 of Ref. 11 for 2.6 (monolayer) ML Fe/11 ML Ni bilayer on Cu(100).

In the second set of simulations, we use the transverse ferromagnetic ground state with the spins aligned along the positive x axis as the initial spin configuration. Snapshots of several spin configurations at increasing times are presented in Fig. 7.

The results of the simulations show that as the system evolves toward equilibrium, the spins rotate and align out of

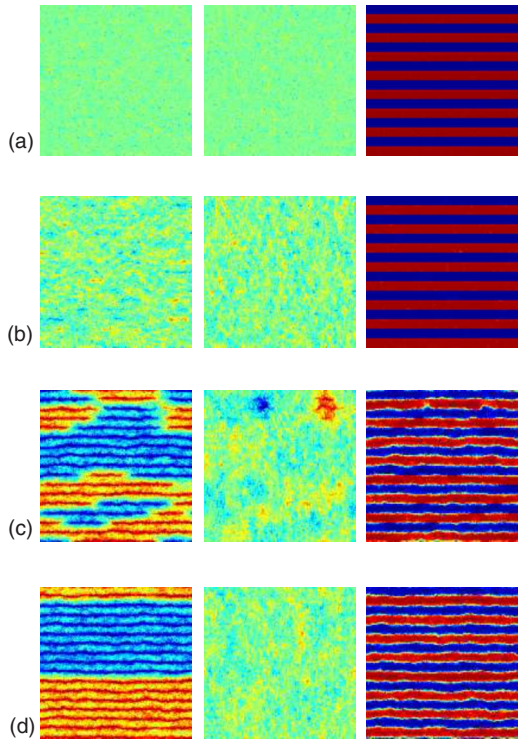

FIG. 5. (Color online) Configurations showing the x, y, and z components of the spins for a quenched system from ordered perpendicular stripes to $T=0.50$ at (a) $t=100$ MCSs, (b) $t=1000$ MCSs, (c) $t=10\,000$ MCSs, and (d) $t=1\times10^6$ MCSs.

plane forming ferromagnetic stripes of width $h\approx8$. While the stripes evolve slowly, by $t=10^6$ MCSs, the stripes are clearly ordered along the x axis parallel to the initial magnetization. As in the previous set of runs, the stripes have a complicated structure and are separated by stripe walls of finite width in which the spins align to form, in this case, a single domain, with a net transverse magnetization.

The final set of simulation results consists of a quench from a random spin configuration and is presented in Fig. 8. While the evolution of this system does not appear to equilibrate even after 10^6 MCSs, nevertheless, we clearly see that as the system evolves the spins align out of plane, forming ferromagnetic stripes of width $h=8$. However, because the initial state does not define a direction for nucleating stripes, the system does not exhibit the orientational order of the previous simulations. Nevertheless, it can be clearly seen that the walls separating the stripes have a finite width, and the spins within the stripe walls are tilted toward the plane in the direction of the stripe walls as in the previous examples.

The differences and similarities between the three different quenches described above are illustrated in the three graphs shown in Fig. 9 which plot the energy, orientational order parameter O_{hv}, and the transverse magnetization as functions of time in MCS for each of the three initial spin configurations. Note that the time axis is shown on a logarithmic scale, where we have chosen to plot ten data points per decade. Figure 9(a) shows the energy for each of the three initial configurations evolving toward a common value. The fact that the energies for each of the three quenches quickly evolve toward a common value despite the fact that

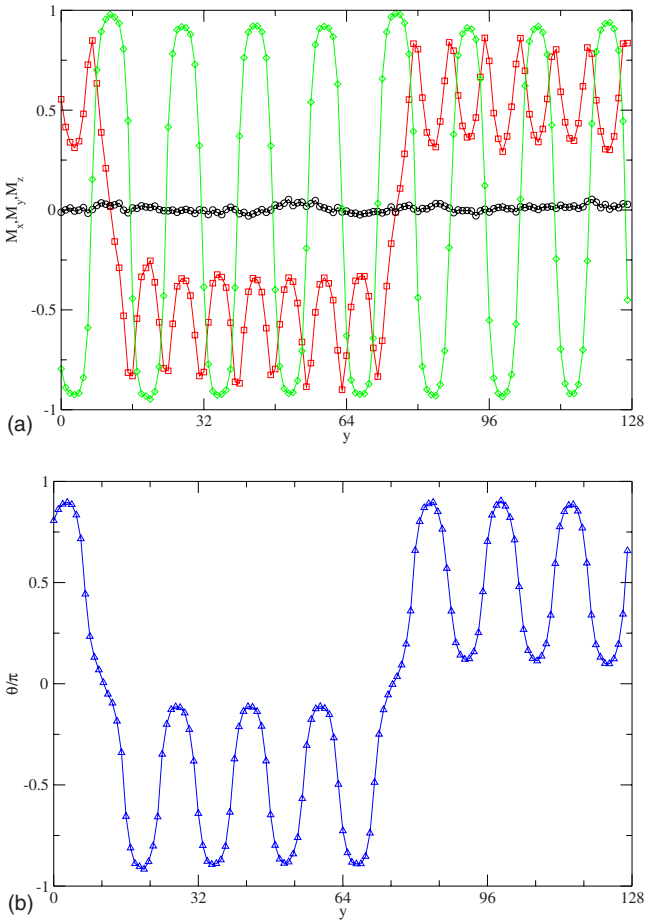

FIG. 6. (Color online) Plots of the magnetization vector averaged along the x axis (parallel to the stripes) as a function of y. (a) shows each of the three components (x, squares; y, circles; z, diamonds) and (b) shows the angle $\theta(y)=\arctan(\langle\sigma_z\rangle/\langle\sigma_x\rangle)$.

the system has clearly not equilibrated may be attributed to the fact that the energy associated with the relative orientation of the stripes represents an extremely small fraction of the total energy and is, in fact, smaller than the energy fluctuations even at this very low temperature.

Figure 9(b) shows the orientational order parameter for the perpendicular stripe and planar ferromagnetic initial spin configurations evolve toward a common value, consistent with the final spin configurations shown in Figs. 5 and 7. The fact that the orientational order parameter for the random initial spin configuration is significantly lower than that of the other two initial spin configurations reflects the observation from Fig. 8 that while the spins have aligned to form the stripe domains, the domains themselves have not ordered along a common axis. This is consistent with previous work[21,38–40] on the dipolar Ising system, in which it is shown that, while the spins align to form stripes relatively quickly from a saturated initial state, the ordering of the stripes along a common axis occurs over a much longer time frame.

The difference between the evolution of the magnetization in Fig. 9(c) for the perpendicular stripe and planar initial spin configurations reflects the fact that final spin configuration shown in Fig. 7 for the planar initial spin configuration consists of a single domain in which the transverse components

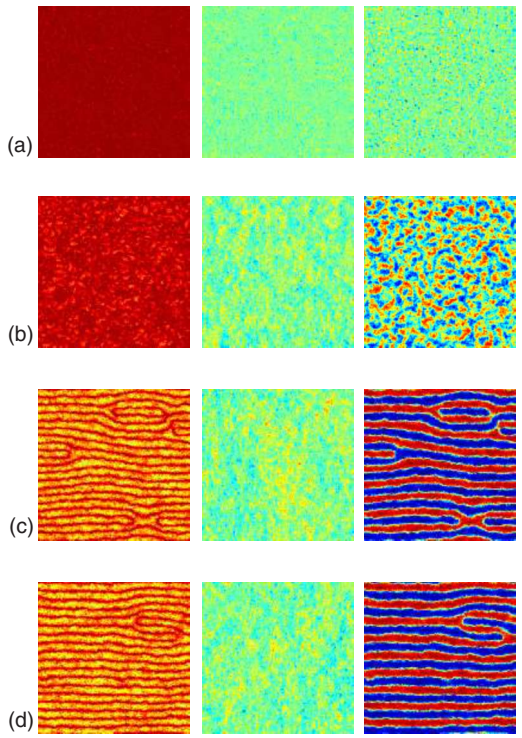

FIG. 7. (Color online) Configurations showing the x, y, and z components of the spins for a quenched system from an in-plane ferromagnetic state to $T=0.50$ at (a) $t=100$ MCSs, (b) $t=1000$ MCSs, (c) $t=10\,000$ MCSs, and (d) $t=1\times10^6$ MCSs. The color map showing how the components of the spins are mapped as in Fig. 1.

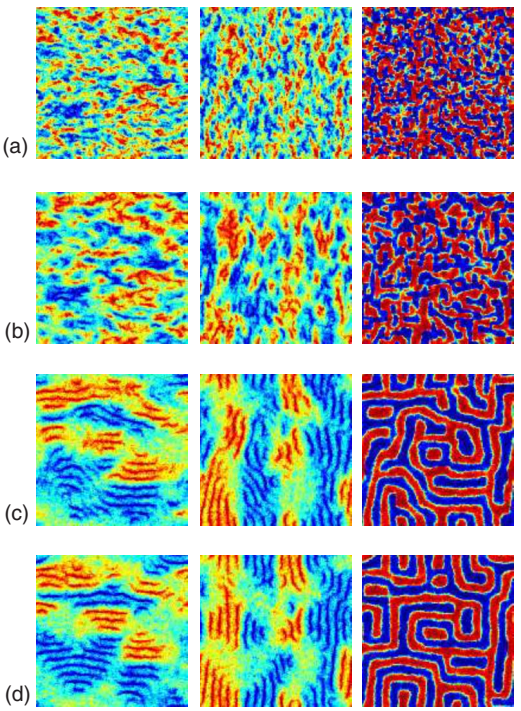

FIG. 8. (Color online) Configurations showing the x, y, and z components of the spins for a quenched system from random to $T=0.50$ at (a) $t=100$ MCSs, (b) $t=1000$ MCSs, (c) $t=10\,000$ MCSs, and (d) $t=1\times10^6$ MCSs. The color map showing how the components of the spins are mapped is as in Fig. 1.

of the spins in stripe walls are aligned in the same direction, while in the case of the initial perpendicular stripe configuration, the final spin configuration consists of two roughly equal regions, one with the transverse magnetization aligned in the positive x direction and the other with the transverse magnetization aligned in the negative x direction. This undoubtedly reflects the fact that while the planar initial spin configuration defines a direction for the transverse magnetization, the perpendicular stripe configuration does not. While the simulations indicate that one of the regions will grow at the expense of the other until it encompasses all the spins, this process will take place very slowly.

The data presented in the graphs shown in Fig. 9 show that the system we are considering is very slow to equilibrate and that even after 10^7 MCSs the state is strongly dependent on the initial conditions. However, despite the equilibration issues, it would appear that for $\kappa=13.0$, the system evolves to an equilibrium with complex magnetic order in which the spins align to form stripes of width $h=8$, but with the spins canted toward the plane. The data therefore seems to imply that at $T=0.5$ the equilibrium phase for $\kappa=13.0$ is indeed a stripe phase, in which the perpendicular component of the magnetization oscillates with a wavelength $\lambda=2h$, but with the spins canted toward the plane in the direction of the stripes. The canted nature of the equilibrium spin configurations gives rise to a net transverse magnetization with a significant contribution to the net magnetization from the spins contained within the narrow region separating adjacent stripes. We refer to this form of magnetic order as a canted stripe configuration and distinguish it from the equilibrium magnetic order observed for $\kappa=20.0$, which we refer to as a perpendicular stripe configuration. In the next section, we present an analysis of the ground state spin configuration that supports these conclusions.

III. GROUND STATE PROPERTIES

The simulation results described in the previous section that, at low temperature close to the reorientation transition, the equilibrium magnetic order consists of a canted stripe configuration in which the spins are aligned at an angle θ to the z axis in a plane normal to one of the lattice axes and parallel to the direction of the stripes. Without loss of generality, we choose the normal to this plane to be the y axis. The angle θ is therefore a periodic function of y only with period $2h$.

Writing

$$\vec{r} = m\hat{x} + n\hat{y}, \tag{9}$$

$$\vec{\sigma} = \cos\theta\hat{z} + \sin\theta\hat{x}, \tag{10}$$

with

$$\theta(m,n) = \theta(n) = \theta(n+2h), \tag{11}$$

the dipolar contribution to the energy given by Eq. (1) may be written as

$$\mathcal{E}_{\text{dip}} = \frac{N\Gamma_0}{2h} + \frac{N}{2h}\sum_{\substack{l_1=1 \\ l_2=1 \\ l_1\neq l_2}}^{2h}\Bigg(\cos[\theta(l_1)-\theta(l_2)]\Gamma_1(|l_1-l_2|) - \frac{3N}{2h}\sum_{\substack{l_1=1 \\ l_2=1}}^{2h}\sin\theta(l_1)\sin\theta(l_2)\Gamma_2(|l_1-l_2|)\Bigg), \tag{12}$$

where Γ_0, $\Gamma_1(l)$, and $\Gamma_2(l)$ are defined as

$$\Gamma_0 = \sum_{mn}{}' \frac{1}{(m^2+4h^2n^2)^{3/2}}, \tag{13a}$$

$$\Gamma_1(l) = \sum_{mn} \frac{1}{[m^2+(2hn+l)^2]^{3/2}}, \tag{13b}$$

$$\Gamma_2(l) = \sum_{mn} \frac{m^2}{[m^2+(2hn+l)^2]^{5/2}}. \tag{13c}$$

These slowly converging sums may be expressed in terms of rapidly convergent sums by means of the Ewald summation technique, thus allowing them to be efficiently calculated numerically. A detailed derivation is presented in the Appendix. The calculation of the interactions Γ_0, $\Gamma_1(l)$, and $\Gamma_2(l)$ means that the energy of any spin configuration described in terms of the $2h$ variables $\theta(l)$ that describe the orientation of the spins relative to the z axis in the magnetic unit cell can be easily evaluated.

More usefully, we can determine the spin configuration that minimizes the energy of the canted stripe phase as a function of the parameters $\mathcal{J}$, κ, and h. Figure 10 shows the ground state (i.e., minimum energy) spin configurations for several values of κ, with the initial spin configuration given by the formula

$$\theta(n) = -\frac{\pi}{20}\sin\left(\frac{\pi n}{h}\right). \tag{14}$$

The results for $\kappa=12.0$, shown in Fig. 10, indicate that while the spins are aligned in the transverse direction, the single site anisotropy induces a small perpendicular component that varies along the y axis of the unit cell. This is also seen in Fig. 11 which plots the angle the spins in the unit cell make with the z axis. The data show that the spins form a ripplelike structure with an approximately sinusoidal variation in the angle. Both Figs. 10 and 11 show that the amplitude of the ripples increases with increasing κ until $\kappa=13.75$ above which the spins are aligned perpendicular to the plane.

This sinusoidal variation of the spins is also reflected in the transverse magnetization plotted as a function of κ in Fig. 12. For $\kappa<11.8$, we see that the transverse magnetization is constant and saturated, corresponding to the planar ferromagnetic ground state spin configuration, with the spins aligned along the x axis. For $\kappa>11.8$, the transverse magnetization begins to decrease corresponding to the formation of the canted stripe ground state spin configuration. The magnetization continues to decrease with increasing κ, as the amplitude of the ripples increases, until at $\kappa=13.6$ the spins are aligned perpendicular to the plane in the perpendicular stripe ground state spin configuration.

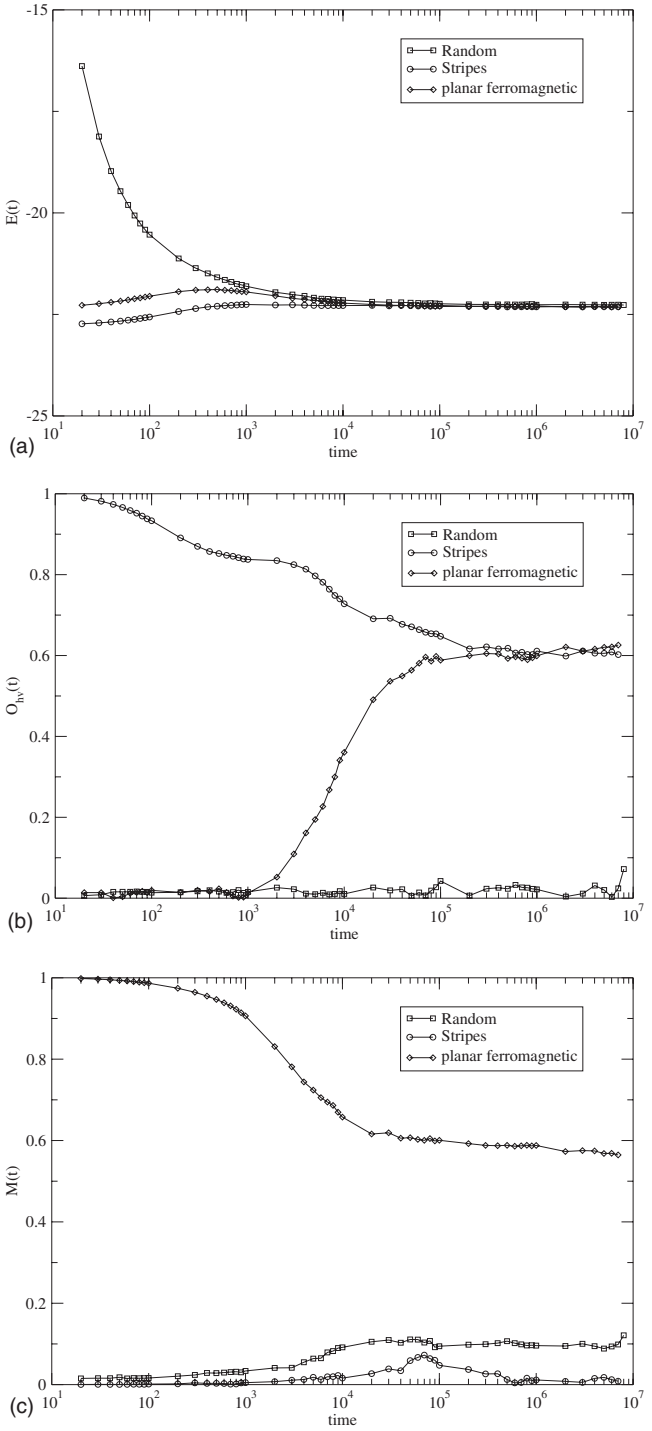

FIG. 9. Plot of the (a) energy, (b) orientational order parameter O_{hv}, and (c) the transverse magnetization for each of the three initial spin configurations. Lines connect successive points as a guide to the eye.

The results obtained from the calculation of the ground state spin configurations show that, at zero temperature, the reorientation from the planar ferromagnetic ground state ($\kappa<11.8$) to the perpendicular stripe ground state ($\kappa>13.6$) is

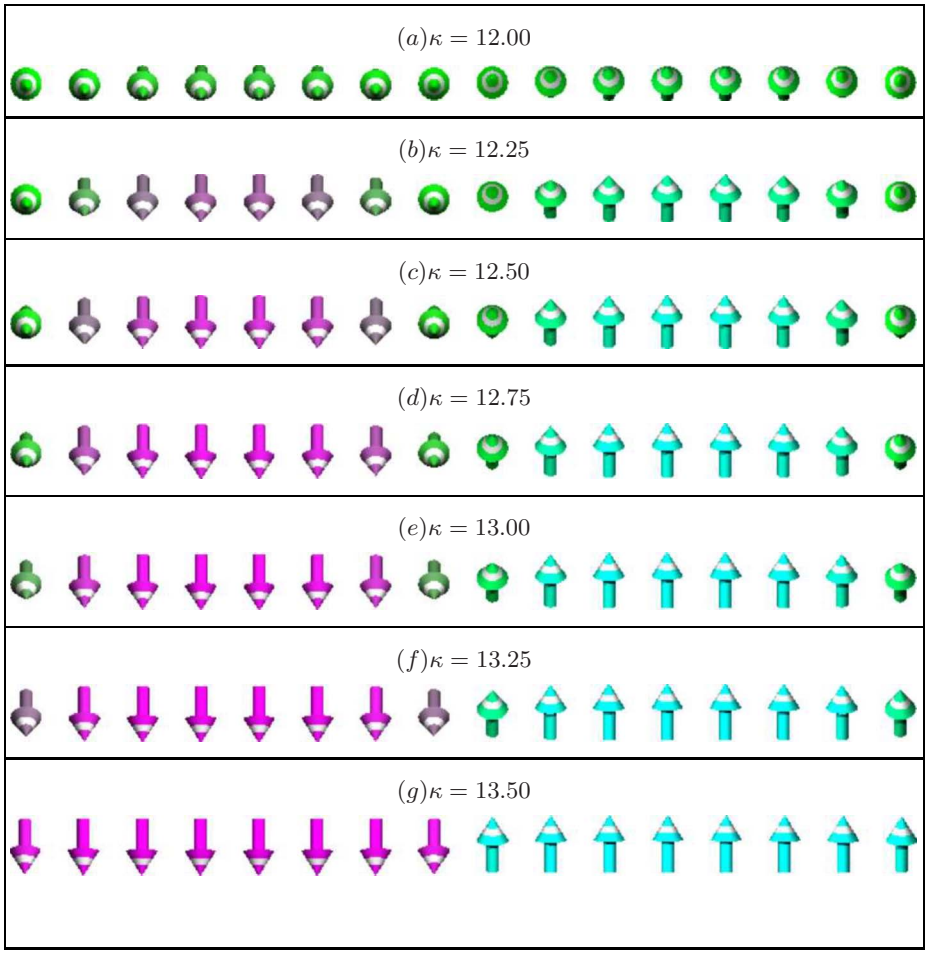

FIG. 10. (Color online) Several equilibrium (minimum energy) spin configurations for $\mathcal{J}=8.9$ and $h=8$ for several values of κ.

mediated by the canted stripe ground state. This is also reflected in the ground state energy plotted as a function of κ in Fig. 13, which also includes the energies of the planar ferromagnetic and perpendicular stripe spin configurations, as given by Eqs. (2) and (3), respectively, for comparison. The data show that there exists a range of κ for which the ground state energy is lower than the energies of both the ferromagnetic and perpendicular spin configurations. In this region, the ground state corresponds to a canted stripe spin configuration.

Thus far, the results presented in this section assume a periodicity $2h=16$. This is based on the results obtained earlier for the dipolar Ising model which gives $h=h^*e^{\mathcal{J}/4}$ with

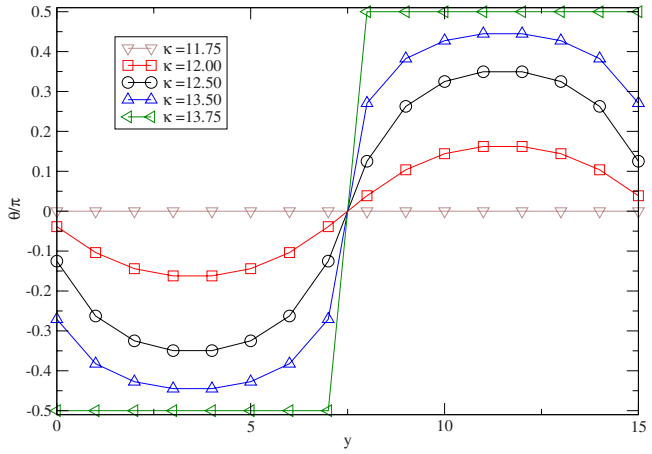

FIG. 11. (Color online) The angle θ of the ground state spin configurations calculated for $\mathcal{J}=8.9$ and $h=8$ plotted for several values of κ.

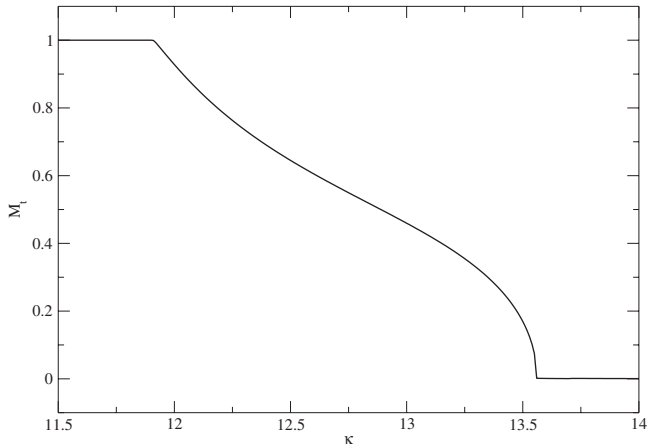

FIG. 12. Transverse magnetization of the canted stripe phase for $h=8$ plotted as a function of κ.

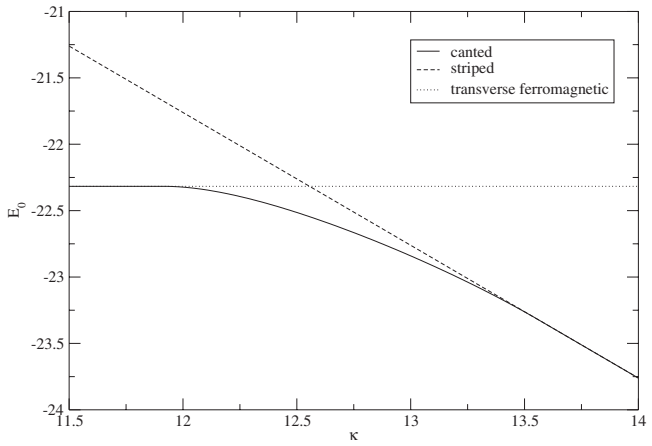

FIG. 13. Ground state energy of the canted stripe phase for $h=8$ plotted as a function of κ. Also shown for comparison are the energies of the transverse ferromagnetic phase and the perpendicular stripe phase.

$h^*=0.871$,[31] which yields a value of $h=8$ for $\mathcal{J}=8.9$. However, while this result is also correct for the perpendicular stripe spin configuration, it is by no means obvious that it extends to the canted stripe spin configuration, since for a given $\mathcal{J}$ and κ, the structure and the energy of the ground state spin configuration will depend on the periodicity in some nontrivial fashion. In Fig. 14 the ground state energy is plotted as a function h for three different values of κ. The graphs show that the ground state energy $E_0(h)$ depends on κ in a nontrivial way. In particular, we see that as κ is reduced from $\kappa=13.5$ to 12.5, the location of the minimum also shifts, indicating that the equilibrium width of the stripes decreases with decreasing κ. Obviously, for the size of systems considered in the present work, the range of h and κ we can consider is somewhat limited and it would be interesting to extend these studies to larger values of $\mathcal{J}$ and correspondingly larger stripe widths.

It is interesting to compare the results of this analysis with the earlier work of Yafet and Gyorgy[18] in which they considered the spin configuration for finite anisotropy Heisenberg model. The analysis of Yafet and Gyorgy is based on the ansatz that the spin configuration describing the stripes can be separated into two regions, the stripe wall region where the spins are assumed to vary sinusoidally with wavelength $\lambda=2w$ and an interior region of width $h-w$ in which the spins are assumed to be aligned in a constant direction, parallel to the z axis. Their approach considers the case that $h \gg 1$. While the present analysis is qualitatively consistent with the result of Yafet and Gyorgy in that h decreases with decreasing κ, the fact that in our analysis we select $\mathcal{J}=8.9$ and hence $h \leqslant 8$ excludes any meaningful quantitative comparison. In the context of the results presented above, the fact that the ansatz employed by Yafet and Gyorgy cannot probe the low amplitude oscillation in σ_z observed in the spin configurations for $\kappa \approx 12.0-12.5$ shown in Figs. 10(a)–10(c) also makes a detailed comparison difficult. Although, it should be noted the ansatz used by Yafet and Gyorgy has been generalized to consider the case of an applied transverse field in which the spins in the interior region are assumed to be canted by some small, uniform angle θ, in the direction of the field.[12] More significant perhaps is the fact that there is no apparent coupling aligning the magnetization in neighboring domains walls, implicit in the present analysis, in the analysis of Yafet and Gyorgy and its generalizations.[12] This arises as a consequence of the assumption that the magnetization in the interior region of the stripe is assumed to be uniform. This implies that the spins inside the stripe walls cannot spontaneously align to give rise to the net transverse magnetization observed in the present analysis. It will be interesting therefore to extend the present

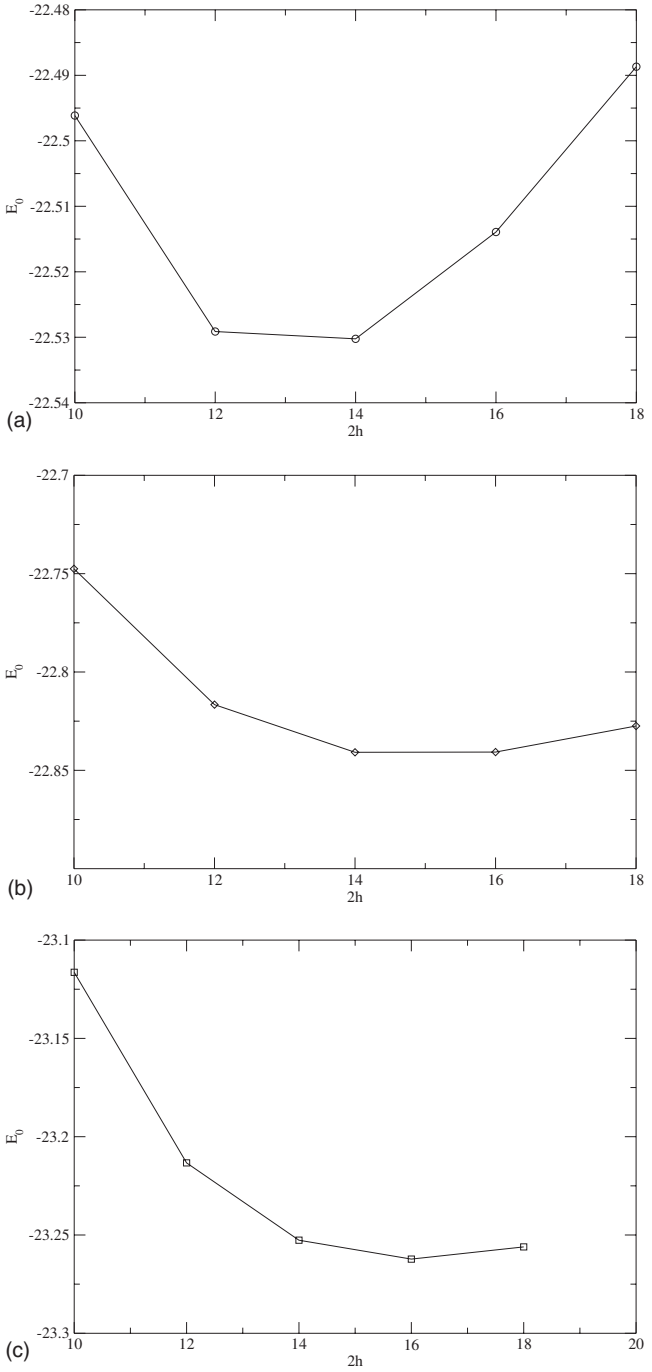

FIG. 14. Ground state energy as a function of the size of the magnetic unit cell $2h$ for several values of κ.

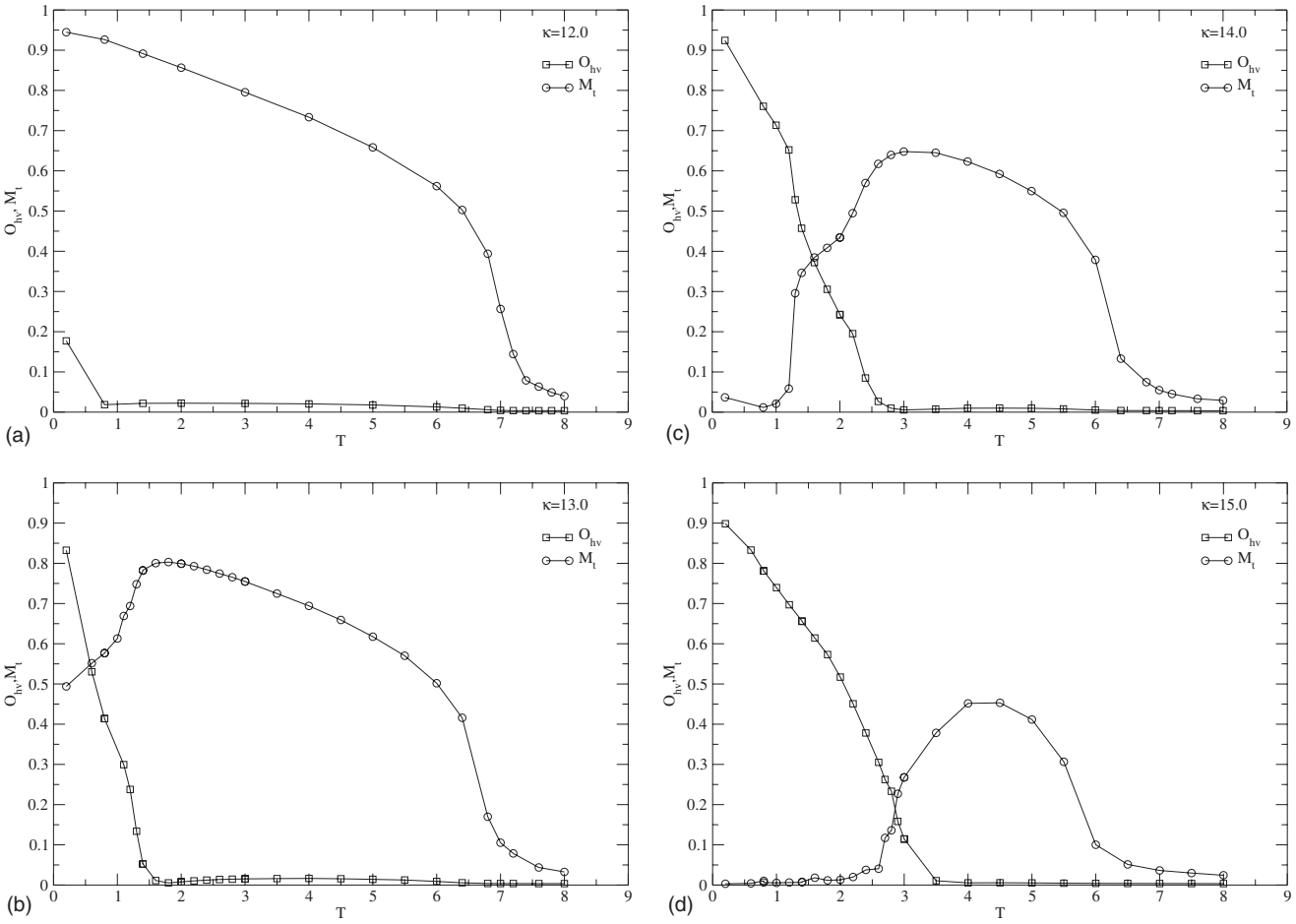

FIG. 15. Plots of the orientational order parameter O_{hv} and the transverse magnetization as a function of the temperature for (a) $\kappa=12.0$, (b) 13.0, (c) 14.0, and (c) 15.0. Note in all cases there exists a range of temperatures for which both order parameters are finite, consistent with the canted nature of the equilibrium spin configuration. Lines connect successive points as a guide to the eye.

work to larger values of $\mathcal{J}$ and hence larger strip widths and to compare the results with the predictions of Yafet and Gyorgy, in a regime where we would expect there to be good quantitative agreement.

IV. PHASE DIAGRAM

From the simulation data presented in Sec. II for $\kappa=0$, we observe that the low temperature phase of the system is planar ferromagnetic with a transition to the paramagnetic phase at $T_c \approx 9.0$. For $\kappa=20.0$, the simulation data show that at low temperature, the equilibrium phase is the smectic stripe phase with a transition to tetragonal phase at $T_0=3.8$, similar to the results obtained from the dipolar Ising model. The transverse magnetization for $\kappa=0.0$ is effectively zero over the entire temperature range studied.

The calculation of the ground state spin configurations shows that for $T=0$, there exist three distinct ground state spin configurations: the planar ferromagnetic ($0.0<\kappa<11.8$), the canted stripe spin configuration ($11.8<\kappa<13.6$), and the perpendicular stripe spin configuration ($\kappa>13.6$). These results are consistent with the simulations described in Sec. II for $\kappa=13.0$ and $T=0.5$ which show the system evolving toward a stripe phase, with a finite orientational order parameter O_{hv}, but with the spins canted toward the plane, giving rise to a finite transverse magnetization. These results are generally consistent with the earlier simulation studies of the dipolar Heisenberg model.[27]

In this section, we present results from an extensive series of Monte Carlo simulations that extend these results over a range of values of κ and T. The methodology for the simulations is similar to that described in Sec. II. However, in order to avoid the equilibration problems identified by our quench studies, we use as a common initial spin configuration for all the simulations a spin configuration in which all the spins are aligned in the xz plane with an angle θ given by

$$\theta(x,y) = -\frac{\pi}{2}\cos\left(\frac{\pi y}{h}\right). \tag{15}$$

We allow the system to equilibrate for 10^5-10^6 MCSs before we collect data every 10–20 MCSs over the next 10^5-10^7 MCSs. The initial spin configuration specified in Eq. (15) appears to allow the system to equilibrate within the first 10^5 MCSs.

In Figs. 15(a)–15(d), we plot the transverse magnetization and the orientational order parameter as a function of temperature for $\kappa=12.0$, 13.0, 14.0, and 15.0. For $\kappa=12.0$ and

$T=0.2$, we see that the transverse magnetization $M_t \approx 0.95$, indicating that the spins are strongly polarized along the x axis. However, we note that the orientational order parameter $O_{hv}=0.18$ is small, but finite, indicating that the system is in the stripe phase but with spins canted toward the plane. This is consistent with the ground state spin configuration shown in Fig. 10(a), which shows a ground state spin configuration with small amplitude ripples along the y axis for $\kappa=12.0$ at $T=0$. As the temperature is increased, however, we see in Fig. 10(a) that O_{hv} drops effectively to zero, while the transverse magnetization remains finite over a much larger temperature range, going to zero at $T \approx 8.0$. These data, along with the ground state calculations presented in Sec. III, indicate that the system undergoes a transition from a striped phase in which the spins are canted toward the plane ($|O_{hv}|>0, |M_t|>0$) to the planar ferromagnetic phase ($|O_{hv}|=0, |M_t|>0$) as the temperature is increased from $T=0.2$ to 0.6 and a second transition from the planar ferromagnetic phase to the paramagnetic phase as the temperature is further increased to $T \approx 8.0$.

For $\kappa=13.0$, simulation data, plotted in Fig. 15(b), show that for $T=0.2$, the transverse magnetization $M_t \approx 0.49$ and the orientational order parameter $O_{hv} \approx 0.83$, indicating that the system is again in the stripe phase with the spins canted toward the plane along the x axis. As the temperature is increased, the orientational order is observed to decrease and the transverse magnetization increase until $T \approx 1.6$, at which point the orientational order parameter goes to zero, indicating that the system is now in the transverse ferromagnetic phase. As the temperature is further increased, the transverse magnetization begins to decrease, going effectively to zero at $T_c \approx 8.4$ at which point the system is in the paramagnetic phase. This interpretation is supported by an examination of sample spin configurations shown in Fig. 16.

For $\kappa=14.0$ and 15.0, simulation data, plotted in Figs. 15(c) and 15(d), respectively, show that for $T=0.2$, the transverse magnetization is essentially zero while the orientational order parameter $O_{hv} \approx 0.9$, indicating that the system is in the stripe phase but with the spins aligned, on average, perpendicular to the plane. As the temperature is increased, O_{hv} decreases; however, before it drops to zero, we see that at $T \approx 1.2$ and 1.8, for $\kappa=14.0$ and 15.0, respectively, the transverse magnetization begins to rise, indicating that the spins are beginning to tilt toward the plane. As the temperature is increased further, the transverse magnetization continues to increase, reflecting the increasing tilt of the spins toward the plane, while the orientational order parameter decreases until, at temperature $T \approx 2.4$ and 3.5, for $\kappa=14.0$ and 15.0, respectively, it drops essentially to zero, indicating that the system has made the transition from the stripe phase to the planar ferromagnetic phase. Once in the ferromagnetic phase, the transverse magnetization begins to decrease with increasing temperature dropping essentially to zero at $T_c \approx 7.1$ for $\kappa=14.0$ and $T_c \approx 6.5$ for $\kappa=15.0$. Again, this interpretation is supported by an examination of sample spin configurations shown for $\kappa=14.0$ in Fig. 17.

The data for $\kappa=14.0$ and 15.0 are particularly interesting as they both show the character of the magnetic order changing abruptly from a perpendicular stripe configuration to a canted stripe configuration on heating over a very narrow temperature range well before the system makes the transition to the planar ferromagnetic phase. This would imply that the three ground state configurations identified in Sec. III for

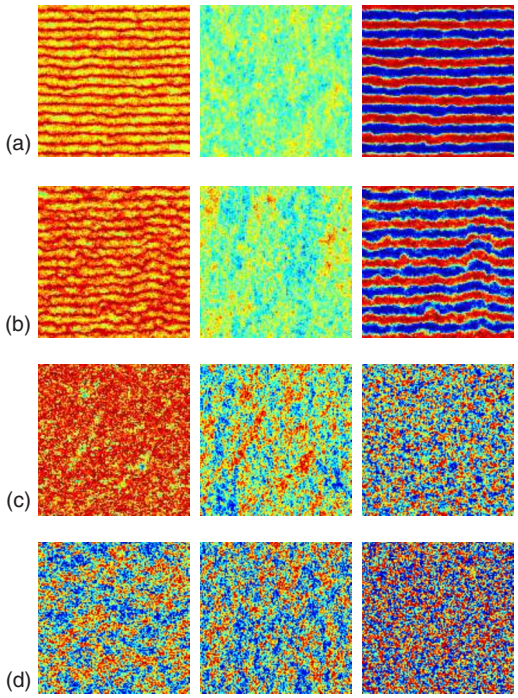

FIG. 16. (Color online) Configurations showing the x, y, and z components of the spins for $\kappa=13$ at (a) $T=0.6$, (b) $T=1.0$, (c) $t=4.5$, and (d) $T=8.0$. The color map showing how the components of the spins are mapped is as in Fig. 1

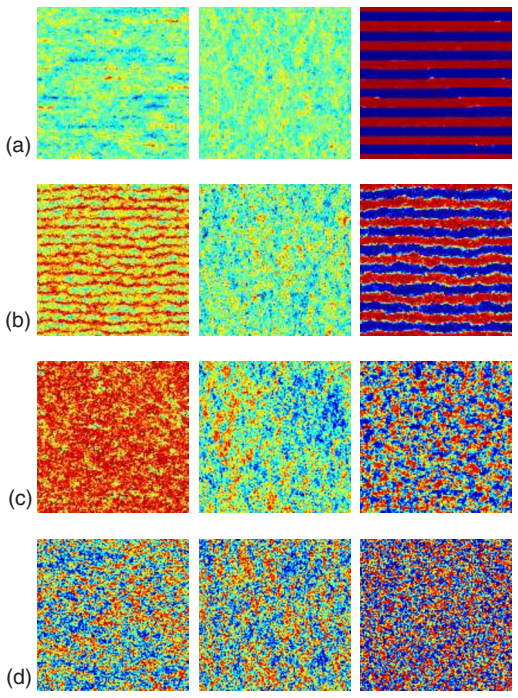

FIG. 17. (Color online) Configurations showing the x, y, and z components of the spins for $\kappa=14$ at (a) $T=0.8$, (b) $T=1.8$, (c) $t=3.5$, and (d) $T=8.0$ The color map showing how the components of the spins are mapped is as in Fig. 1.

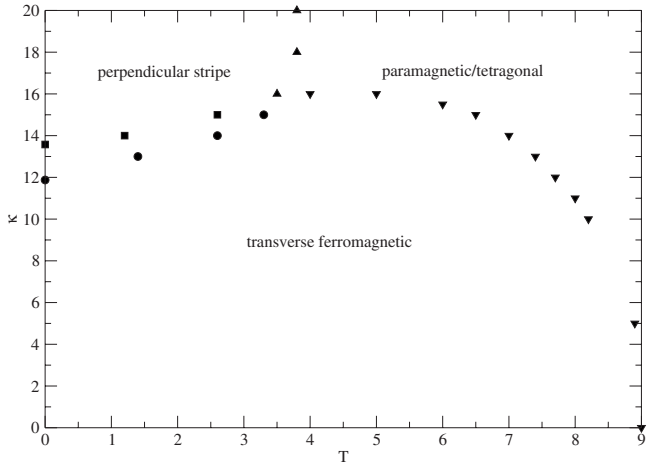

FIG. 18. The phase diagram for the system in the κT plane determined from the values of the orientational order parameter and the transverse magnetization obtained from Monte Carlo simulations and for $T=0$ from numerical studies.

$T=0$ are reflected in the magnetic order observed at finite temperature.

The points separating the three types of magnetic order estimated from the data presented in Fig. 15 together with the results from the ground state calculations presented in Sec. III for $T=0.0$ are shown on the phase diagram in Fig. 18. Also included are the points indicating the transition from the planar ferromagnetic to the tetragonal/paramagnetic phase for $\kappa=0.0$ and from the smectic stripe phase to the tetragonal phase for $\kappa=20.0$, based on the data presented in Sec. II.

Simulation results showing the transverse magnetization as a function of κ calculated for $T=4.0$, 5.0, and 6.0 are shown in Fig. 19(a) and as a function of T for $\kappa=5.0$, 10.0, and 11.0 in Fig. 19(b). In all cases, the orientational order parameter O_{hv} is effectively zero. From the data, we can estimate the transition temperature at which the system makes the transition from the planar ferromagnetic phase to the paramagnetic phase for several values of κ. These points are included on phase diagram of Fig. 18.

In Fig. 20 the orientational order parameter O_{hv} is plotted for $\kappa=16$ and 18 as a function of temperature. The transverse magnetization in this temperature range is effectively zero for both values of κ. We can estimate the temperature at which the orientational order parameter goes effectively to zero indicating that the system has made the transition to the tetragonal/paramagnetic phase. The estimates for the points obtained from these data are included in the phase diagram.

The points delineating the different types of magnetic order observed in our simulations and ground state calculations presented in Fig. 18 show that for $\mathcal{J}=8.9$ and $\kappa>0$, the Heisenberg model exhibits three distinct forms of magnetic order characterized by the two order parameters, namely, the transverse magnetization M_t and the orientational order parameter O_{hv}. That these different forms of magnetic order define different thermodynamic phases and that the lines separating them, implied by Fig. 18, represent phase boundaries is supported by the specific heat data presented in Fig. 21. Figure 21(a) shows a plot of the specific heat for κ

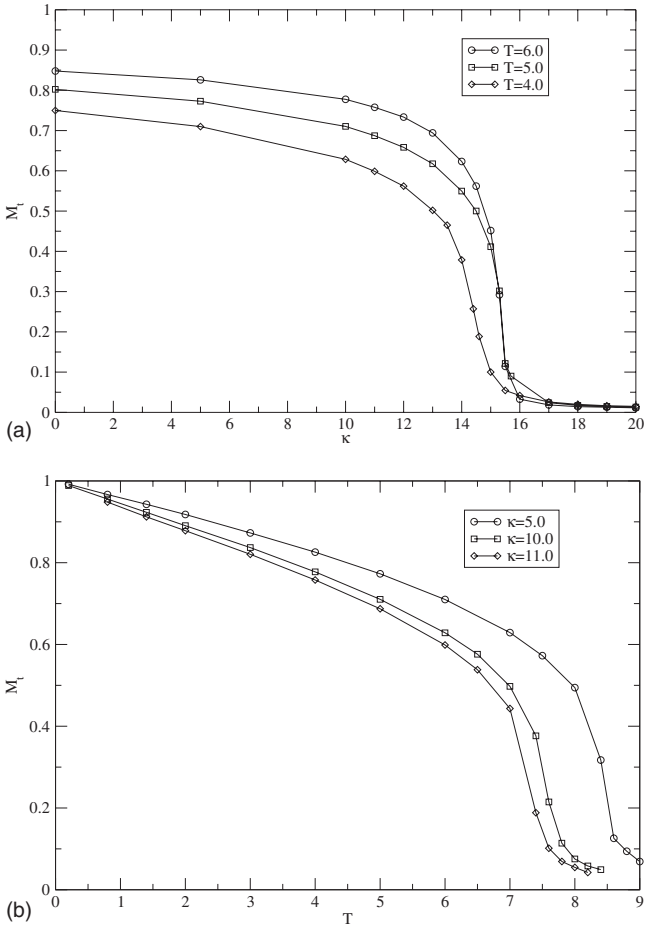

FIG. 19. The transverse magnetization plotted (a) as a function of κ for $T=4.0$, 5.0, and 6.0 and (b) as a function of T for $\kappa=5.0$, 10.0, and 11.0. Lines connect successive points as a guide to the eye.

$=14.0$ calculated as a function of temperature. The data show three well defined peaks corresponding to transition from the perpendicular stripe phase ($|M_t|=0$, $|O_{\rm hv}|\neq 0$) to the canted stripe phase ($|M_t|\neq 0$, $|O_{\rm hv}|\neq 0$), the canted stripe phase to

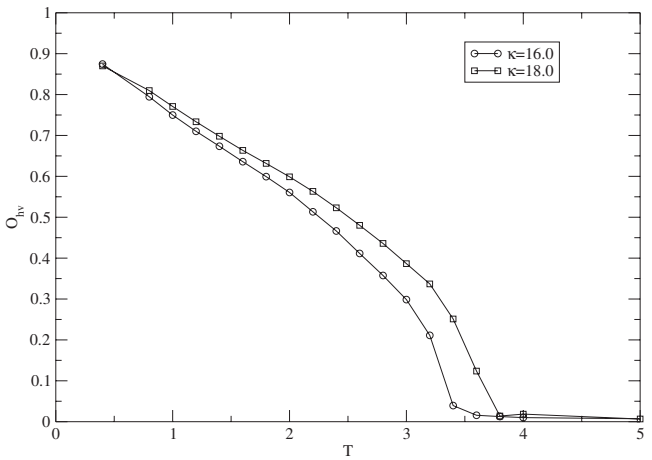

FIG. 20. The orientational order parameter O_{hv} plotted as a function of T for $\kappa=16.0$ and 18.0. Lines connect successive points as a guide to the eye.

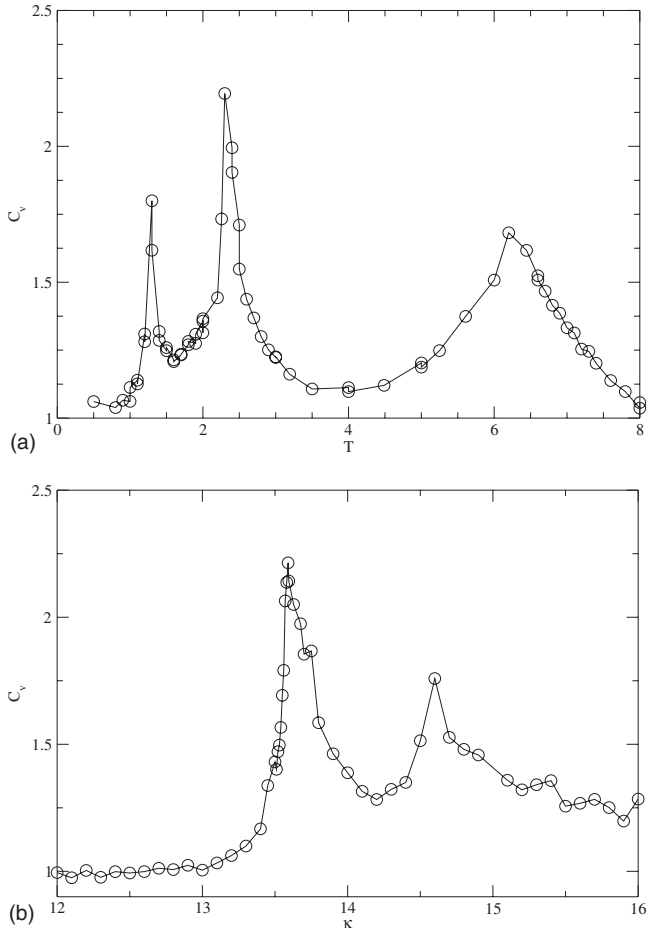

FIG. 21. The specific heat (a) at $\kappa=14$ as a function of temperature and (b) at $T=2.0$ as a function of κ. Lines connect successive points as a guide to the eye.

the planar ferromagnetic phase ($|M_t| \neq 0$, $|O_{\mathrm{hv}}|=0$), and the planar ferromagnetic phase to the tetragonal/paramagnetic phase ($|M_t|=0$, $|O_{\mathrm{hv}}|=0$). Figure 21(b) shows a plot of the specific heat for $T=2.0$ calculated as a function of κ. The data show two well defined peaks corresponding to the transitions from the planar ferromagnetic phase to the canted stripe phase and from the canted stripe phase to the perpendicular stripe phase. One will note that the fluctuations in Figs. 21(a) and 21(b) appear to be larger than in Figs. 3 and 4. This is due to the phase transitions being driven by changes in the magnetization within the stripe walls, rather than within the entire system, and hence the effective size of the system is significantly smaller. We also note that we have not seen any evidence for a phase transition separating the paramagnetic and tetragonal phases.

While the results of the simulations and the ground state calculations provide convincing evidence for the three distinct phases each characterized by a different magnetic order, more detailed simulations on larger systems are needed in order to determine the precise nature of the phase boundaries and to provide a more definitive confirmation of the phase diagram presented in Fig. 18.

V. CONCLUSIONS

In the preceding sections, we have presented the results from both computer simulations and numerical calculations for the two-dimensional ferromagnetic Heisenberg model on a square lattice. The model includes an exchange interaction, a dipolar interaction, and a magnetic anisotropy and is believed to describe many of the essential features of ultrathin magnetic films. The reduced interaction parameters, $\mathcal{J}$ and κ, are defined by Eq. (1) and we consider the specific case $\mathcal{J}=8.9$.[21]

The results show that for a large perpendicular anisotropy ($\kappa=20$), the magnetic properties of the system are qualitatively similar to those observed for the dipolar Ising model.[21] At low temperature, the system orders magnetically into a smectic stripe phase with the spins aligned, on average, perpendicular to the plane. The stripes are oriented along either the x or y axis and the walls separating the stripes are sharply defined. As the temperature increases, the system undergoes a transition to a tetragonal phase and the perpendicular stripes lose their orientational order.

For zero anisotropy, the results show that the low temperature ordered state is a planar ferromagnet with the spins aligned along either the x or y axis with a transition to the paramagnetic phase at $T=9.0\pm0.2$, in reduced units.

For $\kappa=13.0$, close to where we would expect to observe a transition from the perpendicular stripe phase to the planar ferromagnetic phase, we find in both the ground state calculations and Monte Carlo simulations compelling evidence that while the equilibrium phase at low temperature is a stripe phase in which the perpendicular components of the spins align to form stripes oriented along either the x or y axis, the spins are canted toward the xy plane along a common axis parallel to the stripes. These calculations also show that the stripe walls are no longer sharp Ising-like walls but acquire a finite width. The ground state spin configuration is shown in Fig. 10 for several values of κ.

In Sec. IV, we presented the results of a series of Monte Carlo simulations for various values of κ and T. These results together with those presented in Secs. II and III show that the system manifests three distinct types of magnetic order, characterized by the two order parameters, the transverse magnetization M_t, and the orientational order parameter O_{hv}. In Fig. 18, we plot the points in κT phase space that, based on the simulations and ground state calculations, delineate the different types of magnetic order. We note that, as in the case of the Ising model, we have found no evidence for a phase boundary separating the paramagnetic and tetragonal phases and refer to this high temperature region as the tetragonal/paramagnetic phase. Based on these results and specific heat data calculated from further Monte Carlo simulations, we argue that the Heisenberg model for $\mathcal{J}=8.9$ manifests four distinct phases which we refer to as the perpendicular stripe phase, the canted stripe phase, the planar ferromagnetic phase, and the tetragonal/paramagnetic phase. Additional support for this claim is provided by specific heat data.

Figure 18 shows that the canted stripe phase extends over a finite range of κ and temperature and is intermediate between the perpendicular stripe phase and the planar ferro-

magnetic phase. In the canted stripe phase, close to the phase boundary with planar ferromagnetic phase, the spins align to form a spin density wave that is well approximated by a small amplitude, sinusoidal variation in the perpendicular component of the magnetization. As κ increases, and the system approaches the phase boundary with the perpendicular stripe phase, the amplitude of the spin density wave increases and the perpendicular components of the spins at the center of the stripes are close to their saturation value. At this point, the spin configuration more closely resembles the perpendicular stripe configuration, but with a wall of finite width separating the stripes. What is particularly noteworthy in these results is the fact that the spins within the domain walls are observed to align along a common axis, in this case, the x axis, giving rise to a net transverse magnetization. This feature of the canted stripe phase is observed not only in the ground state calculations of Sec. III and the equilibrium Monte Carlo simulations of Sec. IV, but also in the quenches described in Sec. II, suggesting that this is not simply an artifact of the initial conditions and long equilibration times. Ground state calculations also show that the equilibrium stripe width in the canted stripe phase decreases with decreasing stripe κ, consistent with earlier theoretical work.[18] Very recent results from work on smaller systems with smaller stripe widths by Carubelli *et al.*[41] are consistent with the current results in regimes where meaningful comparisons are appropriate.

The results presented in this paper show the same qualitative features of the earlier theoretical work on the both the Ising model[21] and Heisenberg models[18,27] and provide an interesting interpretation of the phase behavior of ultrathin magnetic films in the vicinity of the reorientation transition. However, given the small number of stripes despite the relatively large system size, more detailed simulations on larger systems are required to determine the precise nature of the phase boundaries implied by Fig. 18 and how they connect. That said, while the precise character of the phase boundaries is an interesting and important question, the results presented in this paper provide valuable insight into the nature of the magnetic order close to the reorientation transition. Indeed, it is very tempting to conclude that the canted stripe phase that we observe, separating the perpendicular stripe phase and the transverse ferromagnetic phase, is related in some way to the "pseudogap which possesses complex magnetic structure" referred to by Qiu *et al.*[12] It will be interesting therefore to extend these calculations to larger values of $\mathcal{J}$ and hence larger stripe width. This should provide a much more detailed and comparison with earlier theoretical work[12,18,22,23] as well as provide a closer connection with experimental studies.

ACKNOWLEDGMENTS

This work was supported by the Natural Sciences and Engineering Council of Canada (NSERC). The authors would like to acknowledge SHARCNET and ACEnet for the provision of the computing resources used in this work and the University of Western Ontario Centre for Chemical Physics and SHARCNET for financial support and assistance from Jason Mercer with regard to the three-dimensional visualization of the data.

APPENDIX

The dipolar contribution to the energy of a given spin configuration $\{\vec{\sigma}_i\}$ is given by [Eq. (1)]

$$\mathcal{E}_{\mathrm{dip}} = \sum_{i\neq j}\left(\frac{\vec{\sigma}_i\cdot\vec{\sigma}_j}{|\vec{r}_{ij}|^3} - 3\frac{(\vec{\sigma}_i\cdot\vec{r}_i)(\vec{\sigma}_j\cdot\vec{r}_j)}{|\vec{r}_{ij}|^5}\right). \tag{A1}$$

Writing

$$\vec{r} = m\hat{x} + n\hat{y}, \tag{A2}$$

$$\vec{\sigma} = \cos\theta\hat{z} + \sin\theta\hat{x}, \tag{A3}$$

with

$$\theta(m,n) = \theta(n) = \theta(n+2h), \tag{A4}$$

the dipolar contribution to the energy given by Eq. (A1) may be written as

$$\mathcal{E}_{\mathrm{dip}} = \frac{N\Gamma_0}{2h} + \frac{N}{2h}\sum_{\substack{l_1=1\\ l_2=1\\ l_1\neq l_2}}^{2h}\left(\cos[\theta(l_1)-\theta(l_2)]\Gamma_1(|l_1-l_2|) - \frac{3N}{2h}\sum_{\substack{l_1=1\\ l_2=1}}^{2h}\sin\theta(l_1)\sin\theta(l_2)\Gamma_2(|l_1-l_2|)\right), \tag{A5}$$

with

$$\Gamma_0 = \sum_{mn}{}' \frac{1}{(m^2+4h^2n^2)^{3/2}}, \tag{A6a}$$

$$\Gamma_1(l) = \sum_{mn}\frac{1}{[m^2+(2hn+l)^2]^{3/2}}, \tag{A6b}$$

$$\Gamma_2(l) = \sum_{mn}\frac{m^2}{[m^2+(2hn+l)^2]^{5/2}}. \tag{A6c}$$

Writing $\Gamma_1(l)$ (for $l\neq 0$) as

$$\begin{aligned}\Gamma_1(l) &= \sum_{mn}\frac{1}{[m^2+(2hn+l)^2]^{3/2}}\\ &= \frac{4}{\sqrt{\pi}}\sum_{mn}\int_0^\infty d\rho\rho^2 e^{-\rho^2[m^2+(2hn+l)^2]}\\ &= \frac{4}{\sqrt{\pi}}\sum_{mn}\int_0^\eta d\rho\rho^2 e^{-\rho^2[m^2+(2hn+l)^2]}\\ &\quad + \frac{4}{\sqrt{\pi}}\sum_{mn}\int_\eta^\infty d\rho\rho^2 e^{-\rho^2[m^2+(2hn+l)^2]},\end{aligned} \tag{A7}$$

the second term in Eq. (A7) may be evaluated to give

$$\frac{4}{\sqrt{\pi}}\sum_{mn}\int_{\eta}^{\infty} d\rho\rho^2 e^{-\rho^2[m^2+(2hn+l)^2]} = \sum_{mn}\frac{f_1[\eta\sqrt{m^2+(2hn+l)^2}]}{[m^2+(2hn+l)^2]^{3/2}}, \tag{A8}$$

with

$$f_1(\zeta) = \frac{2\zeta}{\sqrt{\pi}}e^{-\zeta^2} + \mathrm{erfc}(\zeta). \tag{A9}$$

Since $f_1(\zeta)\approx\exp(-\zeta^2)$ for $\zeta\to\infty$, the above series converges rapidly for any reasonable choice of η.

Evaluating the first term in the Eq. (A7) is somewhat more complicated. Using the results that

$$\sum_{m=-\infty}^{\infty} e^{-\rho^2 m^2} = \frac{\sqrt{\pi}}{\rho}\sum_{m=-\infty}^{\infty}\exp\left(-\frac{\pi^2 m^2}{\rho^2}\right), \tag{A10a}$$

$$\sum_{n=-\infty}^{\infty} e^{-\rho^2(2hn+l)^2} = \frac{\sqrt{\pi}}{2h\rho}\sum_{n=-\infty}^{\infty}\exp\left(i\frac{\pi nl}{h}-\frac{\pi^2 n^2}{4h^2\rho^2}\right), \tag{A10b}$$

we can write the first term in the series as

$$\begin{aligned}
&\frac{4}{\sqrt{\pi}}\sum_{mn}\int_0^{\eta} d\rho\rho^2 e^{-\rho^2[m^2+(2hn+l)^2]} \\
&= \frac{2\sqrt{\pi}}{h}\sum_{mn}\exp\left(i\frac{\pi nl}{h}\right)\int_0^{\eta} d\rho\exp\left(-\frac{\pi^2}{\rho^2}\left(\frac{n^2}{4h^2}+m^2\right)\right) \\
&= \frac{2\pi^2}{h}\sum_{mn}\exp\left(i\frac{\pi nl}{h}\right)\sqrt{\frac{n^2}{4h^2}+m^2} \\
&\quad\times\left(\frac{1}{\sqrt{\pi}}\int_{\pi\sqrt{n^2/4h^2+m^2}/\eta}^{\infty}\frac{ds}{s^2}e^{-s^2}\right) \\
&= \frac{2\pi^2}{h}\sum_{mn}\exp\left(i\frac{\pi nl}{h}\right)\sqrt{\left(\frac{n^2}{4h^2}+m^2\right)}g_1\left(\frac{\pi}{\eta}\sqrt{\frac{n^2}{4h^2}+m^2}\right),
\end{aligned} \tag{A11}$$

with

$$g_1(\zeta) = \left(\frac{e^{-\zeta^2}}{\zeta\sqrt{\pi}} - \mathrm{erfc}(\zeta)\right). \tag{A12}$$

Combining the results of Eqs. (A8) and (A11), we obtain (for $l\neq 0$)

$$\begin{aligned}
\Gamma_1(l) &= \sum_{mn}\frac{f_1[\eta\sqrt{m^2+(2hn+l)^2}]}{[m^2+(2hn+l)^2]^{3/2}} \\
&\quad+\frac{2\pi^2}{h}\sum_{mn}\exp\left(i\frac{\pi nl}{h}\right)\sqrt{\left(\frac{n^2}{4h^2}+m^2\right)} \\
&\quad\times g_1\left(\frac{\pi}{\eta}\sqrt{\frac{n^2}{4h^2}+m^2}\right).
\end{aligned} \tag{A13}$$

A similar procedure may be used to express $\Gamma_2(l)$ in terms of rapidly convergent series. Writing $\Gamma_2(l)$ as

$$\begin{aligned}
\Gamma_2(l) &= \sum_{mn}\frac{m^2}{[m^2+(2hn+l)^2]^{5/2}} \\
&= \frac{8}{3\sqrt{\pi}}\sum_{mn} m^2\int_0^{\infty} d\rho\rho^4 e^{-\rho^2[m^2+(2hn+l)^2]} \\
&= \frac{8}{3\sqrt{\pi}}\sum_{mn} m^2\int_0^{\eta} d\rho\rho^4 e^{-\rho^2[m^2+(2hn+l)^2]} \\
&\quad+\frac{8}{3\sqrt{\pi}}\sum_{mn} m^2\int_{\eta}^{\infty} d\rho\rho^4 e^{-\rho^2[m^2+(2hn+l)^2]},
\end{aligned} \tag{A14}$$

the second term in Eq. (A14) may be evaluated to give

$$\begin{aligned}
&\frac{8}{3\sqrt{\pi}}\sum_{mn} m^2\int_{\eta}^{\infty} d\rho\rho^4 e^{-\rho^2[m^2+(2hn+l)^2]} \\
&= \sum_{mn}\frac{m^2 f_2(\eta\sqrt{m^2+(2hn+l)^2})}{[m^2+(2hn+l)^2]^{5/2}},
\end{aligned} \tag{A15}$$

with

$$f_2(\zeta) = \frac{e^{-\zeta^2}}{3\sqrt{\pi}}(6\zeta+4\zeta^3) + \mathrm{erfc}(\zeta). \tag{A16}$$

Since $f_2(\zeta)\approx\exp(-\zeta^2)$ for $\zeta\to\infty$, the above series converges rapidly.

Evaluating the first term in the Eq. (A14) is somewhat more complicated. We recall the result

$$\sum_{m=-\infty}^{\infty} m^2 e^{-\rho^2 m^2} = \frac{\sqrt{\pi}}{2\rho^5}\sum_{m=-\infty}^{\infty}(\rho^2-2m^2\pi^2)\exp\left(-\frac{\pi^2 m^2}{\rho^2}\right). \tag{A17}$$

This result together with Eq. (A10b) allows us to write the first term in the series as

$$\frac{8}{3\sqrt{\pi}}\sum_{mn} m^2 \int_0^{\eta} d\rho \rho^4 e^{-\rho^2[m^2+(2hn+l)^2]}$$
$$= \frac{2\sqrt{\pi}}{3h}\sum_{mn} \exp\left(i\frac{\pi nl}{h}\right)\int_0^{\eta} d\rho\left(1-\frac{2m^2\pi^2}{\rho^2}\right)\exp\left(-\frac{\pi^2}{\rho^2}\left(\frac{n^2}{4h^2}+m^2\right)\right)$$
$$= \frac{2\pi^2}{3h}\sum_{mn} \exp\left(i\frac{\pi nl}{h}\right)\sqrt{\frac{n^2}{4h^2}+m^2}\frac{1}{\sqrt{\pi}}\left(\int_{\pi\sqrt{n^2/4h^2+m^2}/\eta}^{\infty}\frac{ds}{s^2}e^{-s^2}-\frac{2m^2}{\sqrt{\left(m^2+\frac{n^2}{4h^2}\right)}}\int_{\pi\sqrt{n^2/4h^2+m^2}/\eta}^{\infty} ds e^{-s^2}\right)$$
$$= \frac{2\pi^2}{3h}\sum_{mn} \exp\left(i\frac{\pi nl}{h}\right)\left[\sqrt{\left(\frac{n^2}{4h^2}+m^2\right)}g_1\left(\frac{\pi}{\eta}\sqrt{\frac{n^2}{4h^2}+m^2}\right)-\frac{m^2}{\sqrt{\frac{n^2}{4h^2}+m^2}}g_2\left(\frac{\pi}{\eta}\sqrt{\frac{n^2}{4h^2}+m^2}\right)\right], \tag{A18}$$

with

$$g_2(\zeta)=\mathrm{erfc}(\zeta). \tag{A19}$$

Combining Eqs. (A15) and (A18), we obtain the following expression for $\Gamma_2(l)$:

$$\Gamma_2(l)=\sum_{mn}\frac{m^2 f_2(\eta\sqrt{m^2+(2hn+l)^2})}{[m^2+(2hn+l)^2]^{5/2}}+\frac{2\pi^2}{3h}\sum_{mn}\exp\left(i\frac{\pi nl}{h}\right)$$
$$\times\left[\sqrt{\left(\frac{n^2}{4h^2}+m^2\right)}g_1\left(\frac{\pi}{\eta}\sqrt{\frac{n^2}{4h^2}+m^2}\right)\right.$$
$$\left.-\frac{m^2}{\sqrt{\frac{n^2}{4h^2}+m^2}}g_2\left(\frac{\pi}{\eta}\sqrt{\frac{n^2}{4h^2}+m^2}\right)\right]. \tag{A20}$$

The remaining term, Γ_0, may also be evaluated using the techniques described above. Writing

$$\Gamma_0=\sum_{mn}{}'\frac{1}{(m^2+4h^2n^2)^{3/2}}$$
$$=\sum_{mn}{}'\int_0^{\infty} d\rho\rho^2 e^{-\rho^2(m^2+4h^2n^2)}$$
$$=\frac{4}{\sqrt{\pi}}\sum_{mn}{}'\int_0^{\eta} d\rho\rho^2 e^{-\rho^2(m^2+4h^2n^2)}$$
$$+\frac{4}{\sqrt{\pi}}\sum_{mn}{}'\int_{\eta}^{\infty} d\rho\rho^2 e^{-\rho^2(m^2+4h^2n^2)}, \tag{A21}$$

the second term in Eq. (A21) may be evaluated to give

$$\frac{4}{\sqrt{\pi}}\sum_{mn}{}'\int_{\eta}^{\infty} d\rho\rho^2 e^{-\rho^2(m^2+4h^2n^2)}=\sum_{mn}{}'\frac{f_1[\eta\sqrt{m^2+(2hn+l)^2}]}{(m^2+4h^2n^2)^{3/2}}, \tag{A22}$$

with $f_1(\zeta)$ defined in Eq. (A9). The first term may be written as

$$\sum_{mn}{}'\int_0^{\eta} d\rho\rho^2 e^{-\rho^2(m^2+4h^2n^2)}$$
$$=\frac{4}{\sqrt{\pi}}\sum_{mn}\int_0^{\eta} d\rho\rho^2 e^{-\rho^2(m^2+4h^2n^2)}-\frac{4}{\sqrt{\pi}}\int_0^{\eta} d\rho\rho^2$$
$$=\frac{2\pi^2}{h}\sum_{mn}\sqrt{\left(\frac{n^2}{4h^2}+m^2\right)}g_1\left(\frac{\pi}{\eta}\sqrt{\frac{n^2}{4h^2}+m^2}\right)$$
$$-\frac{4}{\sqrt{\pi}}\left(\frac{\eta^3}{3}\right). \tag{A23}$$

Combining Eqs. (A22) and (A23), we can write Γ_0 as

$$\Gamma_0=\sum_{mn}{}'\frac{f_1[\eta\sqrt{m^2+(2hn+l)^2}]}{(m^2+4h^2n^2)^{3/2}}$$
$$+\frac{2\pi^2}{h}\sum_{mn}\sqrt{\left(\frac{n^2}{4h^2}+m^2\right)}g_1\left(\frac{\pi}{\eta}\sqrt{\frac{n^2}{4h^2}+m^2}\right)$$
$$-\frac{4}{\sqrt{\pi}}\left(\frac{\eta^3}{3}\right). \tag{A24}$$

*allanb@uwo.ca

[1] P. J. Jensen and K. H. Bennemann, Surf. Sci. Rep. **61**, 129 (2006).
[2] D. P. Pappas, K. P. Kamper, and H. Hopster, Phys. Rev. Lett. **64**, 3179 (1990).
[3] R. Allenspach, M. Stampanoni, and A. Bischof, Phys. Rev. Lett. **65**, 3344 (1990).
[4] B. Scholz, R. A. Brand, and W. Keune, Phys. Rev. B **50**, 2537

(1994).
[5] F. Baudelet, M.-T. Lin, W. Kuch, K. Meinel, B. Choi, C. M. Schneider, and J. Kirschner, Phys. Rev. B **51**, 12563 (1995).
[6] A. Berger and H. Hopster, Phys. Rev. Lett. **76**, 519 (1996).
[7] H. P. Oepen, M. Speckmann, Y. Millev, and J. Kirschner, Phys. Rev. B **55**, 2752 (1997).
[8] E. Mentz, A. Bauer, T. Günther, and G. Kaindl, Phys. Rev. B **60**, 7379 (1999).
[9] A. Vaterlaus, C. Stamm, U. Maier, M. G. Pini, P. Politi, and D. Pescia, Phys. Rev. Lett. **84**, 2247 (2000).
[10] G. Meyer, A. Bauer, T. Crecelius, I. Mauch, and G. Kaindl, Phys. Rev. B **68**, 212404 (2003).
[11] R. Ramchal, A. K. Schmid, M. Farle, and H. Poppa, Phys. Rev. B **69**, 214401 (2004).
[12] Z. Q. Qiu, J. Pearson, and S. D. Bader, Phys. Rev. Lett. **70**, 1006 (1993).
[13] D. Pescia and V. L. Pokrovsky, Phys. Rev. Lett. **65**, 2599 (1990).
[14] A. Hucht, A. Moschel, and K. D. Usadel, J. Magn. Magn. Mater. **148**, 32 (1995).
[15] S. T. Chui, Phys. Rev. Lett. **74**, 3896 (1995).
[16] Y. Z. Wu, C. Won, A. Scholl, A. Doran, H. W. Zhao, X. F. Jin, and Z. Q. Qiu, Phys. Rev. Lett. **93**, 117205 (2004).
[17] T. Garel and S. Doniach, Phys. Rev. B **26**, 325 (1982).
[18] Y. Yafet and E. M. Gyorgy, Phys. Rev. B **38**, 9145 (1988).
[19] B. Kaplan and G. A. Gehring, J. Magn. Magn. Mater. **128**, 111 (1993).
[20] A. B. MacIsaac, J. P. Whitehead, M. C. Robinson, and K. De'Bell, Phys. Rev. B **51**, 16033 (1995).
[21] I. N. Booth, A. B. MacIsaac, J. P. Whitehead, and K. De'Bell, Phys. Rev. Lett. **75**, 950 (1995).
[22] A. B. Kashuba and V. L. Pokrovsky, Phys. Rev. Lett. **70**, 3155 (1993).
[23] A. B. Kashuba and V. L. Pokrovsky, Phys. Rev. B **48**, 10335 (1993).
[24] A. Berger and H. Hopster, J. Appl. Phys. **79**, 5619 (1996).
[25] D. Venus and M. J. Dunlavy, J. Magn. Magn. Mater. **240**, 365 (2002).
[26] D. Venus, C. S. Arnold, and M. Dunlavy, Phys. Rev. B **60**, 9607 (1999).
[27] F. Matsubara, S. Endoh, and T. Sasaki, J. Phys. Soc. Jpn. **72**, 1326 (2003).
[28] A. B. MacIsaac, J. P. Whitehead, K. De'Bell, and P. H. Poole, Phys. Rev. Lett. **77**, 739 (1996).
[29] A. B. MacIsaac, K. De'Bell, and J. P. Whitehead, Phys. Rev. Lett. **80**, 616 (1998).
[30] In the two previous citations (Refs. 28 and 29), the authors made use of an invalid sampling technique that resulted in the introduction of a temperature dependent effective anisotropy (see Ref. 34); thus, the results presented in these two papers are incorrect and therefore are not relevant to the current work.
[31] J. P. Whitehead and K. De'Bell, J. Phys.: Condens. Matter **6**, L731 (1994).
[32] A. B. MacIsaac, J. P. Whitehead, K. De'Bell, and K. S. Narayanan, Phys. Rev. B **46**, 6387 (1992).
[33] J. P. Whitehead and K. Debell, J. Phys.: Condens. Matter **6**, L731 (1994).
[34] K. De'Bell, A. B. MacIsaac, and J. P. Whitehead, Rev. Mod. Phys. **72**, 225 (2000).
[35] A. B. MacIsaac, M.S. thesis, Memorial University, 1992.
[36] K. De'Bell, A. B. MacIsaac, I. N. Booth, and J. P. Whitehead, Phys. Rev. B **55**, 15108 (1997).
[37] A. B. MacIsaac, *Proceedings of The 16th Annual International Symposium on High Performance Computing Systems and Applications*, HPCS, 2002 (IEEE Computer Society, Moncton, NB, Canada, 2002).
[38] S. Bromley, J. Whitehead, K. D'Bell, and A. MacIsaac, J. Magn. Magn. Mater. **264**, 14 (2003).
[39] Tom Hosiawa and A. B. MacIsaac (unpublished).
[40] A. B. MacIsaac (unpublished).
[41] M. Carubelli, O. V. Billoni, S. Pighin, S. A. Cannas, D. A. Stariolo, and F. A. Tamarit, Phys. Rev. B **77**, 134417 (2008).